Bioactive Materials 35 (2024) 362–381

Contents lists available at ScienceDirect

Bioactive Materials

journal homepage: www.keaipublishing.com/en/journals/bioactive-materials

A cigarette filter-derived biomimetic cardiac niche for myocardial infarction repair

Guofeng Tang [a,b,1], Zhentao Li [b,d,1], Chengbin Ding [a,b], Jiang Zhao [a,b], Xianglong Xing [a,b], Yan Sun [a,b], Xiaozhong Qiu [b,c,**], Leyu Wang [a,b,*]

[a] Biomaterials Research Center, School of Biomedical Engineering, Southern Medical University, Guangzhou, Guangdong, 510515, PR China
[b] Guangdong Provincial Key Laboratory of Construction and Detection in Tissue Engineering, Southern Medical University, Guangzhou, Guangdong, 510515, PR China
[c] School of Basic Medical Science, Southern Medical University, Guangzhou, Guangdong, 510515, PR China
[d] Thoracic and Cardiovascular Surgery, The Tenth Affiliated Hospital, Southern Medical University (Dongguan People's Hospital), Dongguan, Guangdong, 523058, PR China

ARTICLE INFO

Keywords:
Cigarette filter
Cardiac patch
Myocardial infarction
Structural anisotropy
Antioxidative
Angiogenic

ABSTRACT

Cell implantation offers an appealing avenue for heart repair after myocardial infarction (MI). Nevertheless, the implanted cells are subjected to the aberrant myocardial niche, which inhibits cell survival and maturation, posing significant challenges to the ultimate therapeutic outcome. The functional cardiac patches (CPs) have been proved to construct an elastic conductive, antioxidative, and angiogenic microenvironment for rectifying the aberrant microenvironment of the infarcted myocardium. More importantly, inducing implanted cardiomyocytes (CMs) adapted to the anisotropic arrangement of myocardial tissue by bioengineered structural cues within CPs are more conducive to MI repair. Herein, a functional Cig/(TA-Cu) CP served as biomimetic cardiac niche was fabricated based on structural anisotropic cigarette filter by modifying with tannic acid (TA)-chelated Cu^{2+} (TA-Cu complex) via a green method. This CP possessed microstructural anisotropy, electrical conductivity and mechanical properties similar to natural myocardium, which could promote elongation, orientation, maturation, and functionalization of CMs. Besides, the Cig/(TA-Cu) CP could efficiently scavenge reactive oxygen species, reduce CM apoptosis, ultimately facilitating myocardial electrical integration, promoting vascular regeneration and improving cardiac function. Together, our study introduces a functional CP that integrates multimodal cues to create a biomimetic cardiac niche and provides an effective strategy for cardiac repair.

1. Introduction

Myocardial infarction (MI), one of the predominant causes of global morbidity and mortality, derives from obstruction of blood supply to coronary artery [1,2]. Excessive reactive oxygen species (ROS) accumulation explodes in the myocardium after MI and contributes to an aberrant niche, which severely restricts angiogenesis and disrupts cellular homeostasis, leading to massive deaths of cardiomyocytes (CMs) within the infarcted region [3,4]. The initially organized myocardium is replaced by disordered fibrotic scar tissue, which causes abnormal cardiac contraction and irregular electrical signal propagation, eventually resulting in irreversible heart failure [5–7]. Current conventional therapies for MI (such as pharmacological treatments, percutaneous coronary intervention, and bypass graft surgery) only decelerate disease progression rather than restore damaged myocardium function [8,9]. In addition, the shortage of donor hearts for transplantation motivates the urgent need to explore an efficient therapeutic strategy for cardiac repair [10,11].

Cell therapy including pure cell injection and cell sheets offers an appealing avenue for MI repair [12,13]. Healthy and contractile CMs

Peer review under responsibility of KeAi Communications Co., Ltd.
* Corresponding author. Biomaterials Research Center, School of Biomedical Engineering, Southern Medical University, Guangzhou, Guangdong, 510515, PR China.
** Corresponding author. Guangdong Provincial Key Laboratory of Construction and Detection in Tissue Engineering, Southern Medical University, Guangzhou, Guangdong, 510515, PR China.
E-mail addresses: qiuxzh@smu.edu.cn (X. Qiu), wly1026@smu.edu.cn (L. Wang).
[1] These authors contributed equally to this work.

https://doi.org/10.1016/j.bioactmat.2024.02.012
Received 28 November 2023; Received in revised form 24 January 2024; Accepted 7 February 2024

have been confirmed to replace the lost myocardium, which can improve cardiac function through paracrine effects [5,14–16]. Nevertheless, the native cardiac tissue is composed of well-aligned and organized extracellular matrix (ECM), inherently manifesting microstructural anisotropy, elasticity and conductivity [17,18]. The pure implanted cells fail to improve destruction of anisotropic cell structure after MI and are unable to provide mechanical and electrical support [19]. Besides, the pure implanted cells are poor in tolerance of the aberrant myocardial niche, which poses significant challenges to the ultimate therapeutic outcome [20–22]. Fortunately, the functional CPs have been proved to construct an elastic conductive, antioxidative, and angiogenic microenvironment for infarcted myocardium, which are expected to improve cell survival and maturation [8,23,24]. Considerable work has verified that rectifying the aberrant microenvironment of the ECM could attenuate ventricular remodeling and restore cardiac function [18,25,26]. For instance, a smart adhesive Janus hydrogel was fabricated by introducing a redox-responsive interpenetrating network on the porous elastic and conductive hydrogel substrate, which offered a ROS scavenging integrating with mechanical coupled electrical environment for MI repair [27]. Fullerene nanoparticles/alginate hydrogels utilized fullerenol antioxidant nanoparticles to efficiently diminish ROS level within MI area and thus enhance the retention and viability of implanted cells, thereby promoting cardiac function recovery [20]. A strontium ion-containing composite hydrogel released strontium ions to promote angiogenesis and protect CMs [28]. It's noted that mature CMs adapted to the anisotropic arrangement of myocardial tissue are more conducive to MI repair, as evidenced by their enhanced contraction and improved electrical signal propagation, thus promoting the formation of myocardial-like tissue [14]. Cell arrangement induced by bioengineered structural cues within biomaterials is a prevalent approach to establish anisotropic cellular arrangements [18,29–31]. In recent years, massive biosurface topographies containing anisotropic patterns (grooves, aligned fibers) have been constructed by replica casting, chemical etching, electrospinning, and 3D printing techniques [32], while most of these techniques are not only associated with high costs and complex preparation processes, but also difficult to achieve 3D aligned microstructures throughout the interior [33]. Therefore, developing CPs that create a natural myocardium-like niche through a simpler and faster method is desperately desired for MI repair, which effectively directs CMs anisotropic arrangement and provides elastic conductive, antioxidative and angiogenic clues.

Cellulose acetate cigarette filters are commonly overlooked as a useless waste. Interestingly, several researchers have been attracted to conduct studies leveraging the easy surface functionalization of cigarette filters [34,35], while these studies are limited in extracting cellulose acetate from cigarette filters to produce nanofibrous networks by electrospinning [36]. This process is complex and costly, and results in randomly arranged fibers. Considering the consistent orientation fibrous structure from the interior to the exterior of cigarette filter, which resembles the arrangement of natural myocardial tissue, we hypothesize that it has the potential to guide the anisotropic alignment of CMs. Constructing CPs based on this readily available material not only offers the benefits of abundant raw materials and cost-effectiveness but also simplifies and accelerates the preparation of anisotropic topological ECM. Tannic acid (TA) has attracted intensive attention as an ideal candidate to scavenge ROS due to its antioxidant property [37,38]. Specially, the abundant phenolic hydroxyl groups of TA can chelate functional metal ions through dynamic interactions and thus build a functionalized platform [39–41]. Hereinto, Cu^{2+} has been applicated in several studies to promote neovascularization of endothelial cells for diabetic wound healing and bone tissue regeneration [42–44]. Therefore, we expect to construct a functional CP containing TA and Cu^{2+} based on structural anisotropic cigarette filters, which might be a promising candidate for directing CMs orientation, antioxidation, and vascularization in MI treatment.

In this study, we developed a cigarette filter-derived cardiac patch which served as a biomimetic cardiac niche for MI repair. In detail, cellulose acetate cigarette filter was modified with TA-chelated Cu^{2+} (TA-Cu complex) through a greenly convenient one-step method to obtain the scaffold of Cig/(TA-Cu) CP, which basically preserved the ECM-like anisotropic microstructure of filter and enhanced the electrical conductivity due to the introduction of TA-Cu complex. The resultant scaffold exhibited microstructural anisotropy and similar electrical conductivity and mechanical properties to natural myocardium (Scheme 1A), promoting the cellular viability, elongation, orientation, maturation, and functionalization of CMs. Furthermore, the Cig/(TA-Cu) CP could prominently scavenge ROS, promote endothelial cell angiogenesis, provide mechanical support, and reconstruct electrical microenvironment after MI (Scheme 1B), thus enhancing cardiac electrical integration, promoting vascular regeneration and improving the cardiac function (Scheme 1C). Overall, this CP provides multimodal cues to create a biomimetic cardiac niche. The synergy of these elements provides a promising strategy for MI treatment.

2. Materials and methods

2.1. Materials

The discarded cigarette filters utilized in this work were randomly collected from the streets. Alcohol, acetone, hydrazine hydrate, chitosan (deacetylation ≥95%), NaOH, TA, $CuCl_2$ (98%), 2,2-diphenyl-1-picrylhydrazyl (DPPH), Ti $(SO_4)_2$, $FeSO_4$, salicylic acid (SA), H_2SO_4 and H_2O_2 were obtained from Macklin company (Shanghai, China). Nitro blue tetrazolium (NBT) kit was from Zeye Biotech. (Shanghai, China). The Cell Counting Kit-8 assay (CCK-8) was ordered from Dojindo (Japan). The Live-Dead Cell Staining kit and secondary antibodies including Alexa Fluor 568 donkey anti-rabbit IgG and Alexa Fluor 488 donkey anti-mouse IgG were obtained from Invitrogen (US). Cell Navigator F-Actin Labeling Kit, Fluo-4 AM reagent and Wheat Germ Agglutinin (WGA) were purchased from AAT Bioques (USA). The primary antibodies employed in this study, including sarcomeric alpha-actinin (α-actinin), cardiac Troponin T (cTnT), CD206 and CD86 were from Abcam (Britain). α-Smooth Muscle Actin (α-SMA) and von Willebrand factor (vWF) were procured from Boster Biological Technology (Wuhan, China). Connexin-43 (CX43) was ordered from Elabscience (Wuhan, China). 2′,7′-dichlorofluorescein diacetate (DCFH-DA), Superoxide dismutase (SOD) Assay Kit and Malondialdehyde (MDA) Assay Kit were acquired from Solarbio (Beijing, China). Dihydroethidium (DHE) and TUNEL Assay Kit were bought from Beyotime (Shanghai, China). Micro Reduced Glutathione (GSH) Assay Kit was from ACMEC (Shanghai, China).

2.2. Preparation of the scaffolds

The collected cigarette filters were successively treated with ethanol and acetone to remove residual tar and nicotine, and then cleaned with deionized water to obtain acetate fiber bundles. After further treatment with hydrazine hydrate for 10 h at room temperature, these acetate fiber bundles were thoroughly rinsed with deionized water and named CF scaffolds.

For the construction of chitosan-interwoven acetate bundle scaffolds, the obtained CF scaffolds were fully perfused with a chitosan solution (2 wt%, acetic acid as the solvent) under negative pressure. After removing the excess chitosan solution, these chitosan pre-interwoven acetate bundle scaffolds were subjected to low-temperature shaping treatment. Next, the chitosan in these acetate bundle scaffolds was deprotonated using NaOH (1 M) for 4 h. After washing with deionized water, the chitosan-interwoven acetate bundle scaffolds were obtained and named Cig scaffolds.

For the construction of TA&Cu functionalized Cig scaffolds, the prepared Cig scaffolds were incubated in TA solution (2 mg/mL, pH = 8.5) for 10 min. After rinsing with deionized water, these TA-modified

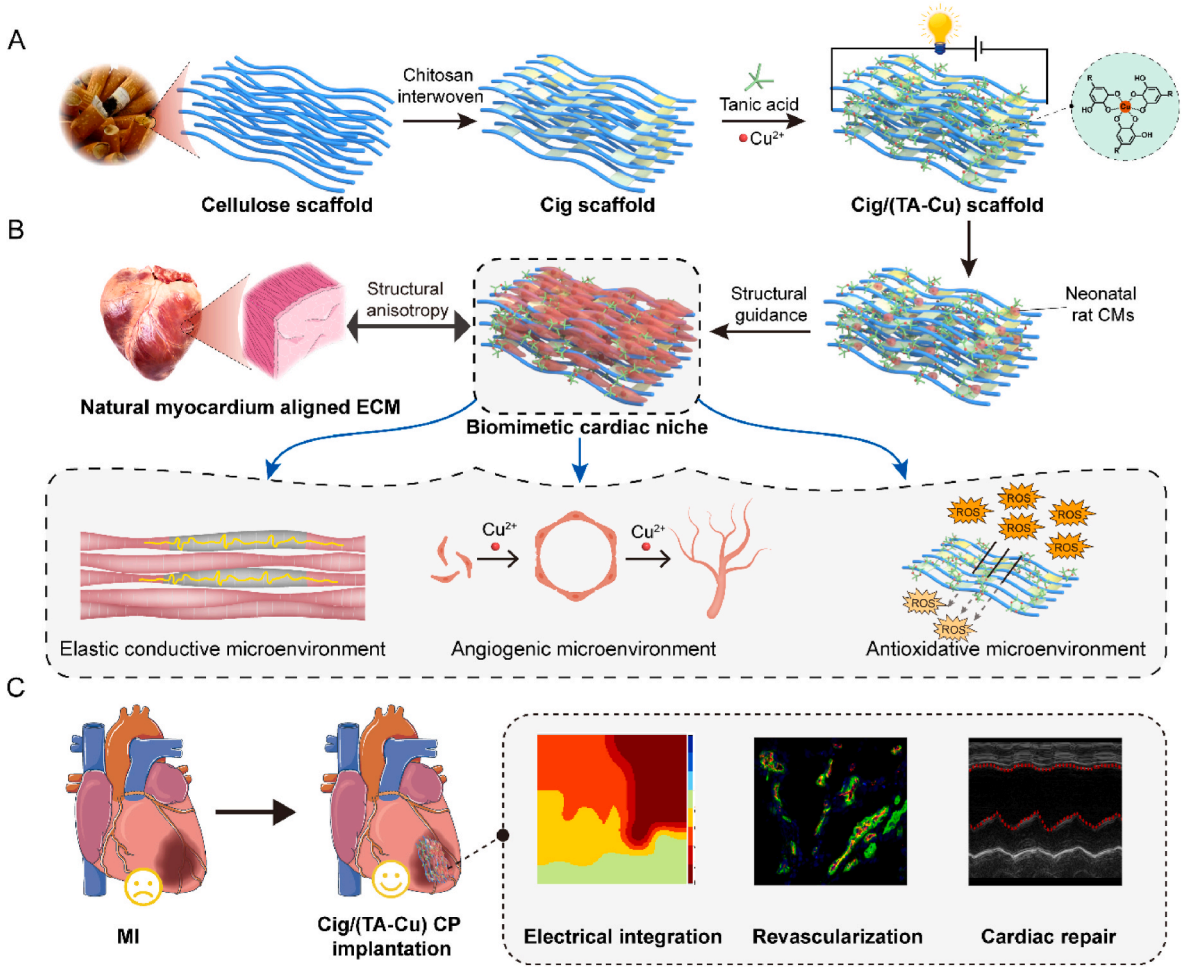

Scheme 1. Schematic illustration about the fabrication of the cigarette filter-derived CP and its repair effect for the infarcted heart. (A) The fabrication of the structural anisotropic scaffold of Cig/(TA-Cu) CP based on waste cigarette filter. (B) The preparation of the Cig/(TA-Cu) CP served as a biomimetic cardiac niche, which constructed a natural myocardial-like structural anisotropic, elastic conductive, antioxidative and angiogenic microenvironment for CMs. (C) The repair effects of Cig/(TA-Cu) CP on MI, including enhancing cardiac electrical integration, promoting revascularization, and improving the cardiac function.

Cig scaffolds were incubated in $CuCl_2$ solution (0.2 mg/mL) for 10 min. Next, NaOH solution (1 M) was dropwise into the above reaction system and the solution pH was calibrated to 8.5, triggering the coordination of TA and Cu^{2+}. After rinsing with deionized water to regulate the pH to 7~7.5, these obtained Cig scaffolds were named Cig/TA scaffolds and Cig/(TA-Cu) scaffolds according to their components.

2.3. Characterization of the cigarette filter-derived scaffolds

The morphology of different scaffolds was examined using scanning electron microscope (SEM, H-7650, Hitachi, Japan) with an acceleration voltage of 5 kV. Surface topology and roughness of scaffolds were characterized using Atomic Force Microscope (AFM, Bruker Dimension Icon, Germany). The element mappings and elemental compositions were scrutinized through SEM coupled with energy-dispersive spectroscopy (EDS, S-3000 N, Hitachi, Japan) and X-ray photoelectron spectroscopy (XPS, Thermo Scientific K-Alpha, USA), respectively. The chemical coordination of the scaffolds was ascertained by Fourier transform infrared spectrophotometry (FTIR, Nicolet iS10, Thermo Scientific) across the wave number spanning from 4000 to 500 cm^{-1}.

The mechanical properties of each scaffold with cylindrical shape (diameter: 4.5 mm, height: 2 mm) were tested at a strain of 150 mm/min with deformation reaching up to 80% using an Instron universal testing system (Instron 34SC-1, USA). Cyclic compression tests were carried out at 50% strain and 150 mm/min for 100 cycles.

Conductivity assessments were conducted on an electrochemical workstation (CorrTest Instruments, China). The electrical conductivity of different scaffolds was determined from cyclic voltammetry (CV) measurements and calculated according to the equation: σ (S/m) = $1/\rho$, $R = \rho L/S$ (σ: electrical conductivity, ρ: electrical resistivity, R: resistance, L: electrode spacing, S: contact area between scaffold and electrode). Electrochemical impedance spectroscopy analysis were conducted over the frequency range spanning from 0.1 to 1000 Hz. Electrochemical impedance analysis was performed over the frequency spectrum ranging from 0.1 to 1000 Hz. The scaffolds were connected to a 3 V power source and a green LED in series to form a closed circuit to monitor current changes by brightness changes and quantified by calculating 8-bit grayscale values using ImageJ software.

The electrical output of the scaffolds was measured by an experiment setup which principled as previous literature reported [45]. First, two pieces of insulating substrates were affixed onto the clamps of an Instron universal tester (Instron 34SC-1, USA), which were subsequently covered with two pieces of copper foil. Conductive wires were led out between the insulating substrates and the copper foil. The sample was then positioned at a plate equipped with a loading cell. A constant pressure was applied to the sample at a fixed frequency using the Instron universal tester. The conductive wires were connected to a programmable electrometer (Keithley DMM7510), and the open-circuit voltage and short-circuit current of the scaffolds were recorded using the Keithley DMM7510 equipped with MATLAB software.

2.4. Biocompatibility of CMs on cigarette filter-derived scaffolds

All the experiments were approved and conducted in accordance with the regulations for animal procedures of the Southern Medical University Animal Ethics Committee (SYXK(Guangdong)2021-0167). Neonatal rat CMs were isolated from the hearts of neonatal Sprague-Dawley (SD) rats aged 1–3 days. Briefly, upon harvesting the rat hearts, extraneous pericardial and atrial tissues were removed. The hearts were then subjected to enzymatic digestion using 0.25% trypsin (Sigma, USA) and 0.1% type II collagenase (Sigma) respectively. Afterwards, the cells were dispersed into single-cell suspension and pre-plated in culture dishes for 2 h to remove fibroblasts. The CMs were collected from the supernatant of pre-plated culture dishes and inoculated onto scaffolds or glass slides, culturing in Dulbecco's modified Eagle's medium (DMEM, GIBCO) supplemented with 15% fetal bovine serum (FBS, Excell Bio) and 1% penicillin/streptomycin. The purity of neonatal rat CMs was >96%, which was analyzed by flow cytometry. Briefly, isolated neonatal rat CMs were fixed in 4% paraformaldehyde (PFA) for 15 min and then permeabilized with 0.2% Triton X-100 for 15 min. After blocked with 2% bovine serum albumin (BSA), the cells were stained with cTnT-AF647 (ab314677, dilution 1:500) for 30 min at room temperature and the unstained neonatal rat CMs were considered as the blank control. Finally, all samples were analyzed by CytoFLEX Platform (Beckman Coulter).

The viability of CMs on various scaffolds was evaluated by live/dead staining and CCK-8 assay after culturing for 3 days and 7 days. Typically, CMs cultured on scaffolds were incubated in Calcein-AM (green fluoresce, represents viable cells)/ethidium homodimer-III (red fluoresce, represents dead cells) staining media at 37 °C for 30 min in darkness and then visualized by laser scanning confocal microscope (LSCM, Nikon A1, Japan). The quantitative cell viability was calculated as the proportion of viable cells relative to the total cell population. The CCK-8 assay was conducted following the manufacturer's guidelines. In detail, primary CMs were inoculated in 96-well culture plates and grown in medium with extracts of different scaffolds for 3 days and 7 days. Subsequently, 100 μL CCK8 staining working solution (10 μL CCK-8 solution + 90 μL DMEM) was introduced to each well and incubated for 1 h at 37 °C under 5% CO_2. Absorbance of each well was then determined at 450 nm using a microplate reader (SYNERGY H, BioTek).

2.5. Detection of cellular morphology on cigarette filter-derived scaffolds

At 7 days of cultivation, CMs on various scaffolds were rinsed with PBS and subsequently fixed in 2.5% glutaraldehyde at 4 °C overnight. Then the fixed samples were sequentially dehydrated using ethanol gradient (50%, 70%, 85%, 90%, and 100%) and critical point-dried. After staining with dioxin and lead citrate, cellular morphologies were observed under SEM (H-7650, Hitachi, Japan).

2.6. Cellular immunofluorescence analysis

To detect the level of cardiac proteins, neonatal rat CMs were isolated and cultivated on various scaffolds. At day 7 after culture, samples were fixed in 4% PFA at 4 °C overnight, followed by permeabilized with 0.2% Triton X-100 for 15 min. After blocking nonspecific binding with 2% BSA for 2 h, the samples were labeled with primary antibodies: rabbit anti-CX43 (E-AB-70097, dilution 1:200) and mouse anti-α-actinin (ab9465, dilution 1:250) at 4 °C overnight. After the primary antibodies were removed, the samples were stained with fluorophore-conjugated secondary antibodies: Alexa Fluor 488 donkey anti-mouse IgG (A21202, dilution 1:500) and Alexa Fluor 568 donkey anti-rabbit IgG (A10042, dilution 1:500) for 2 h at room temperature. Finally, all samples were dyed with 4′,6′-diamidino-2-phenylindole (DAPI) and imaged under LSCM (Nikon A1, Japan). For detecting cytoskeleton organization, samples were treated with fluorescein-isothiocyanate-conjugated phalloidin (40734ES75, dilution 1:500) and incubated in darkness for 30 min. The fluorescent images were captured in five random fields of view for each sample. The distribution of CMs nuclei orientation angles were determined by analyzing cytoskeleton fluorescent images using Image J.

2.7. Measurement of calcium transient

Intracellular Ca^{2+} transients within CMs on different scaffolds were monitored by calcium indicator assay kit. After 5 days of cultivation, all samples were probed with Fluo-4 AM working solution (3 μM Fluo-4 AM and 0.4 mg/mL Pluronic F127, HBSS buffer as the solvent) for 40 min at 37 °C. The samples were subsequently rinsed with buffer solution and the calcium current were recorded using fluorescence microscope (Olympus, BX53, Japan) at a rate of 15 frames/s. Fluorescence intensity (F) was then standardized against the baseline intensity (F0), and the alterations in calcium current over time were graphically represented by ImageJ software.

2.8. Spontaneous beating analysis

The dynamic contractions of CMs on the scaffolds were recorded by an optical microscope (Nikon, ECL TPSE Ts2R) at a rate of 13 frames/s. The resulting videos were then analyzed using Image J software to extract and characterize the beating signals.

2.9. ROS scavenging capability of the cigarette filter-derived scaffolds in vitro

2.9.1. DPPH scavenging ability

100 mg scaffolds were incubated with 1 mL DPPH solution (100 μM, methanol as solvent) at room temperature for 1.5 h in darkness. Afterwards, the supernatant of reacted solution was poured into a standard cuvette to measure the absorbance at 517 nm using UV–vis spectrophotometer (Evolution 300, Thermo Scientific). The scavenging capacity of scaffolds was quantified by the following equation:

$$\text{DPPH scavenging effect}\ (\%) = \frac{A_{control} - A_{sample}}{A_{control}} \times 100\%$$

$A_{control}$ is the absorbance of blank group (DPPH only), and A_{sample} is the absorbance of scaffold groups (DPPH + scaffold).

2.9.2. $O_2^{\bullet-}$ scavenging ability

The $O_2^{\bullet-}$ scavenging efficiency of various scaffolds was measured via calculating the inhibitory ratio of NBT photoreduction using the SOD assay kit, supported by previous literature [46]. Briefly, 100 mg scaffolds were blended with 1 mL NBT working solution and riboflavin solution following the manufacturer's protocol under constant and intense illumination for 20 min, and the absorbance of the supernatant was detected at 560 nm. Percentage inhibition was determined as following formula:

$$O_2^{\bullet-}\ \text{scavenging effect}\ (\%) = \left(1 - \frac{A_{sample} - A_{negative}}{A_{positive} - A_{negative}}\right) \times 100\%$$

A_{sample}, $A_{negative}$, and $A_{positive}$ denote the absorbances of the sample, negative control, and positive control, respectively.

2.9.3. H_2O_2 scavenging ability

First, 100 mg scaffolds were incubated with 1 mL H_2O_2 (1 mM) at 37 °C for 30 min. Subsequently, 500 μL resultant supernatant was mixed with 1 mL Ti $(SO_4)_2$ solution (prepared by mixing 1.33 mL 24% Ti $(SO_4)_2$ with 8.33 mL H_2SO_4 in 50 mL of deionized water) to react for 30 min. The absorbance at 405 nm was then quantified, and the percentage of inhibition was quantified using the subsequent formula:

$$H_2O_2\ \text{scavenging effect}\ (\%) = \frac{A_{control} - A_{sample}}{A_{control}} \times 100\%$$

2.9.4. •OH scavenging ability

The •OH which could be detected by SA, was generated by a Fenton reaction between $FeSO_4$ (2 mM) and H_2O_2 (5 mM). Specifically, different scaffolds were incubated with Fe^{2+}/H_2O_2 system and SA at 37 °C for 30 min. Finally, the absorbance of the mixture supernatant was recorded at 510 nm. The •OH scavenging efficiency was performed using the following equation:

$$\bullet\text{OH scavenging effect}\ (\%) = \frac{A_{control}\text{-}A_{sample}}{A_{control}} \times 100\%$$

2.10. Cellular ROS scavenging activity of the cigarette filter-derived scaffolds

The intracellular ROS and $O_2^{\bullet-}$ was assessed by DCFH-DA and DHE fluorescent staining, respectively. Rat cardiomyoblasts (H9C2 cells) were seeded in 24-well plates and then were cocultured with different scaffolds and 600 μM H_2O_2 for 4 h. After washed with DMEM three times, cells were incubated with DHE or DCFH-DA staining solution (dilution 1:1000) at 37 °C for 30 min, and then were carefully rinsed with PBS three times. Finally, all cells were stained with Hoechst (#33342, Solarbio Biotech.) and imaged under LSCM (Nikon A1, Japan).

2.11. Cell viability, migration and tube formation of endothelial cells

The proliferation of human umbilical vein endothelial cells (HUVECs) cultivated on scaffolds was detected by Live/Dead staining and CCK-8 assay following the procedure described above. A scratch wound method was employed to assess HUVEC migration. HUVECs were inoculated in six-well plates and cultured until reaching confluence to form monolayer, which was subsequently scratched with the pipette tip to create a defined wound area. After the detached cells were removed, adherent cells were incubated with scaffolds floated in the DMEM medium without FBS. The scratch images of HUVECs were captured at the designated time (0, 12, and 24 h) using a microscope (Nikon, ECL TPSE Ts2R). The migration rate was quantified as the percentage decrease in the final scratch width relative to the initial width. For the tube formation assay, a 96-well plate was precoated with 50 μL Matrigel (Corning, USA) and incubated at 37 °C for 30 min. Then every 3×10^4 HUVECs containing 100 μL culture solution were inoculated on Matrigel, and subsequently incubated with 5 mg scaffolds. After culturing for 5 h, the cells were fixed with 4% PFA and subsequently stained with fluorescein-isothiocyanate-conjugated phalloidin. The fluorescent images were captured by microscope (Olympus, BX53, Japan) in Z-stack mode. Quantitative meshes and segment length of the formed tube networks in different groups were analyzed by ImageJ software.

2.12. Establishment of MI model and implantation of cigarette filter-derived CPs

All animal surgical procedures received approval from the Southern Medical University Animal Ethics Committee. 7-8-week-old male SD rats (weight 230 ± 10 g) were randomly assigned to six groups including Sham group, MI group, CMs group (pure CMs injection), Cig CP group (Cig scaffold loaded CMs), Cig/TA CP group (Cig/TA scaffold loaded CMs), and Cig/(TA-Cu) CP group (Cig/(TA-Cu) scaffold loaded CMs). The rat MI model was carried out as previously detailed [47,48]. In brief, following thoracotomy, the left anterior descending artery (LAD) was ligated with 7-0 surgical sutures at a position 1–2 mm inferior to the left atrial appendage. The myocardium below the ligation point transitioned from a vibrant red to a pale, indicating successful establishment of MI. Subsequently, different CPs were implanted onto the epicardium within the infarcted area and fixed along the edges using 7-0 sutures. In the CMs group, neonatal rat CMs were injected at three points surrounding the left ventricular (LV) infarction area. The Sham group was performed the same thoracotomy procedure without LAD ligation.

2.13. Enzyme-linked immunosorbent assay (ELISA)

After 3 days of surgery, the blood of rats was collected from the LV and centrifuged at 3000 rpm for 20 min at 4 °C. The supernatant (a pale yellow clear liquid) was then isolated to measure cTnT level by the Rat cTnT ELISA kit (MEIMIAN, China) following the manufacturer's guidelines. After the addition of the stop solution, absorbance values (at 450 nm) was measured using a microplate reader (SYNERGY H, BioTek).

2.14. Determination of apoptosis and ROS level at the infarcted area

After surgery for 3 days, the rat hearts in each group were rapidly harvested to ensure tissue freshness. DCFH-DA (ROS probe) and DHE (superoxide anion probe) staining of cardiac sections were applied to evaluate the antioxidative capability of the heart tissues in each group. Briefly, cardiac sections were washed with PBS and then labeled with DCFH-DA or DHE probe working solution (dilution 1:1000) in the dark at 37 °C for 30 min. After carefully washed with PBS, the cardiac sections were stained with DAPI and the fluorescence images were immediately captured using LSCM (Nikon A1, Japan). Next, a Tissue ROS detection kit (DHE) (BestBio, China) was utilized to further quantify DHE levels of cardiac tissue in each group. In detail, 50 mg freshly collected infarcted cardiac tissue was thoroughly mixed with 1 mL homogenization buffer. The resulting mixture underwent centrifugation at 100×*g* for 3 min at 4 °C to collect the supernatant, which was incubated with DHE probe (dilution 1:1000) at 37 °C for 30 min. The fluorescence intensity was monitored using a fluorescence microplate reader (SYNERGY H, BioTek) at excitation and emission wavelengths of 500 and 610 nm, respectively. The protein concentration of samples was determined using a BCA protein assay kit (Fude biotech.). Finally, the ratio of fluorescence intensity to protein concentration was defined as the relative ROS intensity.

For evaluating the level of oxidative stress *in vivo*, the activities of SOD and GSH-Px, and the concentration of MDA were assessed by corresponding assay kits. After CPs implantation for 3 days, freshly collected infarcted heart tissues in each group were homogenized with the extraction buffer, and the supernatant obtained post-centrifugation was used as the test substance. Subsequent experimental procedures were conducted consistent with the manufacturer's guidelines.

The cell apoptosis within the infarcted zone was evaluated using the TUNEL staining assay after 3 days of surgery. Briefly, after fixed with 4% PFA, cardiac frozen sections were first incubated with 0.5% Triton X-100 for 5 min and then stained with 50 μL TUNEL reaction solution (5 μL TdT enzyme + 45 μL label solution) for 1 h at 37 °C in darkness. Cardiac sections were finally counterstained with DAPI and visualized by LSCM (Nikon A1, Japan).

2.15. Epicardial activation mapping

To evaluate the propagation of electrical signals between healthy and infarcted myocardium in each group, a 64-channel electrode array mapping system (MappingLab, Oxfordshire, UK) was utilized to measure epicardial electrical activation. At 28 days after CPs implantation, all rats were euthanized and their hearts were promptly gathered, which were immediately connected to a Langendorff perfusion system. A multi-electrode array comprising 64 electrodes was positioned at the boundary area between the healthy and infarcted myocardium to record spontaneous local field potentials. A stimulus electrode was then placed on the epicardium directly beneath the left atrial appendage to deliver electrical pulses of 4 V and 5 Hz for recording the local field potentials and activation times under stimulation conditions. The electrical conduction heat maps were generated and the conduction velocities were analyzed

using EMapScope software.

2.16. Echocardiographic evaluation

At 7 days and 28 days after surgery, transthoracic echocardiography was conducted on the rats in each group using ultrasound imaging machine (Vevo2100, Visual Sonics, USA) to evaluate the LV function. After the rats were anesthetized using isoflurane, their M-mode echocardiograms from short-axis views were captured with a 14 MHz ultrasound probe. The typical cardiac functional parameters such as left ventricular internal diameter at end-diastole (LVIDd), left ventricular internal diameter at end-systole (LVIDs), left ventricular ejection fraction (EF), and left ventricular fractional shortening (FS) were systematically measured and analyzed. $FS = (LVIDd - LVIDs)/LVIDd \times 100\%$, $EF = (LVIDd^3 - LVIDs^3)/LVIDd^3 \times 100\%$.

2.17. Histological assessment

28 days after CPs implantation, cardiac tissues of all rats were harvested and cut into 8 μm-thick frozen sections for subsequent experiments. Masson's trichrome staining was carried out consistent with the manufacturer's instructions to observe myocardial fibrosis, and the images of the whole heart-section were acquired under microscope (Olympus, Japan) in Image Stitching mode. Infarct wall thickness and infarct area were measured using ImageJ software. Infarct area was determined as the proportion of infarct tissue circumference to the entire LV inner circumference.

For immunofluorescence staining of cardiac sections, the experimental procedure was consistent with that of the cell experiments. In brief, cardiac sections from each group were sequentially incubated with primary antibodies (4 °C, overnight), secondary antibodies (37 °C, 2 h), and DAPI, followed by observation under LSCM (Nikon A1, Japan). The primary antibodies were used including: i) mouse anti-α-actinin (ab9465, dilution 1:250) and rabbit anti-CX43 (E-AB-70097, dilution 1:200) to detect the expression of cardiac specific proteins, ii) mouse anti-α smooth muscle actin (α-SMA) (BM0002, dilution 1:250) and rabbit anti-vWF (PB9273-boster, dilution 1:300) to assess the vascular density in the infarcted area, iii) mouse anti-cTnT (ab10214, dilution 1:500) and WGA-FITC (2970071, dilution 1:200) to evaluate the size and function of CMs, and iv) CD86 (ab220188, dilution 1:200) and CD206 (ab64693, dilution 1:200) to determine the inflammatory level.

2.18. Statistical analysis

All experimental results were analyzed and graphed by GraphPad Prism 8 and Origin 2018 software. The data were presented as mean ± standard deviation (SD). Statistical comparisons were executed through one-way analysis of variance (ANOVA) with post hoc Tukey's test, and two-way ANOVA. Statistical significance was denoted as follows: $^*p < 0.05$; $^{**}p < 0.01$; $^{***}p < 0.001$.

3. Results and discussion

3.1. Fabrication and characterization of the cigarette filter-derived scaffolds

The collected waste cigarette filters were successively treated with ethanol and acetone to remove residual tar and nicotine until the appearance changed from deep brown to white (Fig. S1A). After the simple treatment with hydrazine hydrate and deionized water, acetate fiber bundles (noted by CF scaffold) were obtained, which distinctly preserved the inherent structural orientation of the cellulose acetate cigarette filters (Fig. S2A). As shown in Fig. S1C, the Cig scaffold was fabricated through perfusing the CF scaffold with chitosan solution and triggering the deprotonation of chitosan molecules by NaOH to interweave the acetate bundles [49]. Based on the hydrogen bonding and electrostatic interactions between chitosan and TA, the Cig/TA scaffold was obtained by incubating Cig scaffold with TA solution. Then the Cig/(TA-Cu) scaffold was constructed based on the chelate complex of TA and Cu^{2+} (Fig. S1D).

The ultrastructure of different scaffolds was observed by SEM. As shown in Fig. 1A and Fig. S2A, all scaffolds exhibited anisotropic fibrous structure and rougher surface occurred in Cig/TA and Cig/(TA-Cu) scaffolds, indicating that the surface modification of TA and TA-Cu complex didn't destroy the inherent orientation structure of cellulose acetate cigarette filters but enhanced their surface roughness. AFM was utilized to further measure the surface roughness of different scaffolds. The surface of the CF and Cig scaffolds was comparatively smooth and flat whereas the Cig/TA and Cig/(TA-Cu) scaffolds were noticeably rougher (Fig. 1B, Fig. S2B). The root-mean-square roughness (Rq value) of the CF, Cig, Cig/TA, and Cig/(TA-Cu) scaffolds was approximately 16 nm, 50 nm, 115 nm, and 229 nm, respectively (Fig. S2C). The results verified that the roughness increased after surface modification and the highest surface roughness appeared in Cig/(TA-Cu) scaffold, which was due to the coordination interaction between TA and Cu^{2+}. Interestingly, it has been reported that the rough surfaces favored CMs adhesion and growth via influencing the dynamics of integrin-extracellular matrix complexes [50,51]. Accordingly, the Cig/(TA-Cu) scaffold might be considered as an enhancer of CMs adhesion and growth, making it a promising candidate for further application in tissue engineering patches.

Next, the elemental distribution of different scaffolds was examined by SEM-EDS analysis to verify the effectiveness of surface modifications. The additional presence of N element was detected in the Cig, Cig/TA and Cig/(TA-Cu) scaffolds, indicating that chitosan was successfully infused. In particular, it was clearly observed that the additional Cu element uniformly dispersed on the Cig/(TA-Cu) scaffold (Fig. 1C, Fig. S3), which suggested the effective surface modification of TA-Cu complex. The results of XPS spectroscopy revealed a new peak (Cu2p, approximately 930–950 eV) appeared in the Cig/(TA-Cu) scaffold (Fig. S4), which was consistent with the EDS analysis.

The scaffolds of CPs with appropriate mechanical properties can provide mechanical support to repair the rigid and fragile hearts after MI. Firstly, an appropriate elastic modulus resembling natural myocardium can promote the synchronous contraction of CMs, and secondly, a robust fatigue resistance is crucial for maintaining stable cardiac systole and diastole post-implantation onto the infarcted heart [52]. Here, we measured the mechanical properties of various scaffolds by compression tests. There was no visible deformation in appearance under the pressures of 500 g and 200 g horizontally and vertically (Figs. S6A–B). The stress-strain curves showed that the elastic modulus increased with the surface modification of TA and TA-Cu complex compared to the Cig scaffold. This phenomenon could be explained that the introduced TA could crosslink with chitosan through hydrogen bonding and electrostatic interactions, which increased the interwoven structures of chitosan between acetate fiber bundles. The elastic modulus of Cig/TA and Cig/(TA-Cu) scaffolds was 117.8 ± 13.5 kPa and 117.9 ± 12.3 kPa respectively (Fig. 1D and E), which aligned with the range of natural myocardium stiffness (20–500 kPa) [53]. Furthermore, the cyclic compression test was conducted to evaluate the mechanical stability of different scaffolds. After 100 cycles of 50% compress strain, all scaffolds exhibited minor stress loss, suggesting prominent fatigue resistance (Fig. 1F, Figs. S6C–D).

Previous studies have demonstrated that conductive CPs can restore electrical conduction for myocardial tissue after MI [54,55]. The electrical properties of different scaffolds were evaluated by cyclic voltammetry and electrochemical impedance spectroscopy. The electrical conductivity of the Cig, Cig/TA and Cig/(TA-Cu) scaffolds was $(6.0 \pm 0.7) \times 10^{-3}$ S/m, $(8.0 \pm 1.0) \times 10^{-3}$ S/m, $(10.0 \pm 1.6) \times 10^{-3}$ S/m respectively, which corresponded to the natural myocardial tissue (ranging from 5.0×10^{-3} to 1.6×10^{-1} S/m) (Fig. 1G and H). With the modification of TA-Cu complex, the electrical conductivity of scaffolds

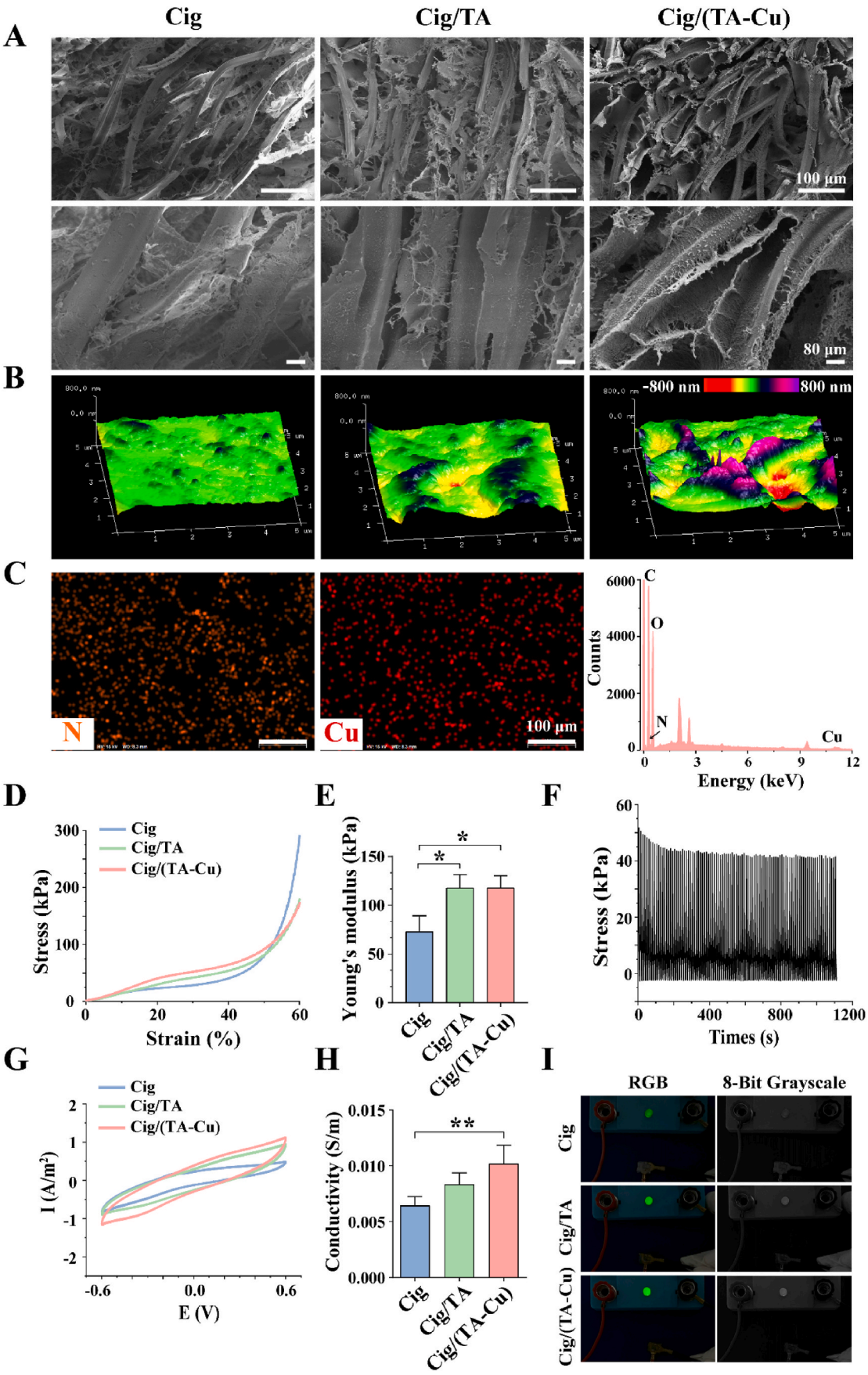

(caption on next page)

Fig. 1. Characterization of different scaffolds. (A) SEM images of Cig, Cig/TA and Cig/(TA-Cu) scaffolds. Up in each group: Low magnification images; Bottom in each group: High magnification images. (B) Spatial topography of different scaffolds measured by AFM. (C) SEM-EDS elemental mappings (left: N element; middle: Cu element) and EDS spectral analysis (right) of Cig/(TA-Cu) scaffold. (D–E) Stress-strain curves (D) and Young's modulus (E) of Cig, Cig/TA and Cig/(TA-Cu) scaffold (n = 3). (F) Cyclic compression tests of Cig/(TA-Cu) scaffolds. Each sample was compressed to a strain of 50% at a rate of 150 mm/min for 100 cycles. (G–H) The cyclic voltammogram curves (G) and conductivities (H) of different scaffolds (n = 4). * and ** represent $p < 0.05$ and $p < 0.01$ between the selected groups. (I) RGB and 8-bit grayscale images of different scaffolds, which connected to an electrical circuit containing a green LED bulb at one side and a 3 V power source at the other side.

significantly increased, which might be explained that the coordination network between TA and Cu^{2+} effectively introduced Cu^{2+} into the scaffold, and the scaffold with an anisotropic 3D network structure provided a tough and stable electron transport network for Cu^{2+} [56]. To monitor the effects of scaffolds on the current changes, different scaffolds were connected to a pair of batteries and a LED in series to form a closed circuit. The results showed that Cig, Cig/TA and Cig/(TA-Cu) scaffolds could illuminate the LED and the brightness increased sequentially (Fig. 1I, Fig. S7B). Interestingly, based on the presence of oriented non-centrosymmetric crystal structure in chitosan and cellulose acetate [45,57], the Cig/(TA-Cu) scaffold could produce electric dipole moments and thus exhibited a discernible piezoelectric effect, which spontaneously generated an open-circuit voltage of approximately 0.2 V and a short-circuit current of 1.8 μA when compressed to 50% strain (Figs. S7C–D). This piezoelectric effect might emulate the electrophysiological environment of CMs more accurately for cardiac tissue engineering.

3.2. Biomimetic Cig/(TA-Cu) scaffold promoted growth and orientation of CMs

The cylindrical scaffolds were sectioned into thin slices with a thickness of 600 μm in longitudinal planes via a Leica CM1950 cryostat (Germany) for further experiments (Figs. S9A–B). F-actin staining of H9C2 cells cultured on scaffolds demonstrated that there were more favorable cell adhesion and alignment in the Cig scaffold compared to the CF scaffold (Fig. S9D), which might be explained that: i) The positively charged properties of chitosan molecules were more conceive to cell adhesion. ii) Chitosan-interwoven acetate bundles displayed a more stable anisotropic structure, which could more efficiently regulate the growth behavior of the cells. Next, we selected chitosan-interwoven scaffolds including Cig, Cig/TA and Cig/(TA-Cu) scaffolds to continue the experiments.

To determine the biocompatibility of different scaffolds for CMs, live/dead staining and CCK-8 assay were performed. After neonatal rat CMs were cultivated on scaffolds for 3 days and 7 days, extensive cell adhesion, robust growth (green), and negligible cell death (red) were observed in the Cig, Cig/TA and Cig/(TA-Cu) scaffolds, suggesting good biocompatibility (Fig. 2A and B). This similar good biocompatibility was also observed in CCK-8 assay (Fig. 2C). Furthermore, the morphology of CMs in scaffolds was examined by SEM. At 7 days of culture, well spreading and continuous CMs were observed on the Cig/TA and Cig/(TA-Cu) scaffolds, while CMs remained poor spreading on the Cig scaffold. It is noted that a confluent monolayer of CMs was formed on the Cig/(TA-Cu) scaffold (Fig. 2D), which resembled a cell sheet and might influence the functionalization and synchronous contraction of CMs. This good biocompatibility of the Cig/(TA-Cu) scaffold could be interpreted that the TA-chelated Cu^{2+} functionalized platform on the structural anisotropic scaffold provided a more stable and rougher interface to the cells, which could serve as facilitator for cell adhesion and spread [52,58].

For exploring the elongation and orientation of CMs in different scaffolds, F-actin staining was conducted after 7 days of culture (Fig. 2E). Compared to the glass slide group, CMs on the scaffolds (especially on the Cig/(TA-Cu) scaffold) exhibited much better spreading and robust F-actin bundles. In addition, the F-actin fibers in most of CMs on Cig/(TA-Cu) scaffold exhibited along one direction whereas randomly distributed in glass slide group. Quantitative analysis of cell orientation and cytoskeletal area revealed that CMs on the Cig/(TA-Cu) scaffold exhibited the narrowest direction range and the largest cytoskeletal area, representing the greatest orientation and the most notable elongation (Fig. 2E and F). This difference in cellular orientation might be due to the variations in the conductivity and surface roughness of the scaffolds, which leads to the difference of CMs extension and maturation, potentially resulting in a longitudinal orientation closer to that of natural CMs. Fig. 2G schematically illustrated the differential impacts of various scaffolds on CMs, which might be explained by following factors: i, Cig/(TA-Cu) scaffold possessed stably structural anisotropic ECM fibers, which could structurally achieve cascading regulation of CM alignment and growth. ii, The introduction of TA-chelated Cu^{2+} functionalized platform provided an elastic and conductive microenvironment for the growth and interconnection of CMs.

3.3. Biomimetic Cig/(TA-Cu) scaffold facilitated maturation and functionalization of CMs

To determine the effects of different scaffolds on CMs maturation, we examined the expression levels of heart-specific proteins including α-actinin, which plays essential role in cardiac contraction [59], and CX43, which is closely involved in electrical contraction coupling of the myocardium and synchronized heart activity [60,61]. After 7 days of cultivation, the primary CMs on the Cig scaffold exhibited round shape with scarce intact sarcomeres (α-actinin) and sparse intercellular connections (CX43 positive coverage area), while the CMs on the Cig/TA scaffold and especially on the Cig/(TA-Cu) scaffold displayed abundant mature sarcomere structures and dense cell-to-cell coupling (Fig. 3A). Quantitative analysis of the α-actinin and CX43 positive areas were substantially increased in the Cig/(TA-Cu) scaffold compared to the Cig scaffold (Fig. 3C and D), indicating that Cig/(TA-Cu) scaffold could substantially enhance intercellular connection and expedite the maturation of CMs.

The synchronized and rapid propagation of transient calcium signals, which leads to excellent spontaneous contraction, is also vital for CM functionalization [62]. To monitor the impact of various scaffolds on the calcium activity of CMs, primary CMs were cultured on scaffolds up to 5 days and the calcium signal propagation was tracked by a Fluo-4 AM fluorescent calcium indicator (Movie S1). At three different randomly selected points, disordered and asynchronous intracellular calcium signals was observed in the Cig scaffold. Conversely, robust, high-frequency and synchronized Ca^{2+} flow signals occurred in the Cig/TA and Cig/(TA-Cu) scaffolds. In particular, CMs on the Cig/(TA-Cu) scaffold exhibited the fastest and the most rhythmic Ca^{2+} fluctuations, suggesting a functional cardiac symbiont was formed between the mature CMs and Cig/(TA-Cu) scaffold [63] (Fig. 3B–E, and F).

Collectively, these outcomes suggested that the Cig/(TA-Cu) scaffold could facilitate the growth, maturation, intercellular communication and functionalization of CMs. This might be interpreted that TA-chelated Cu^{2+} functionalized platform on the Cig/(TA-Cu) scaffold constructed an anisotropic elastic and conductive microenvironment reminiscent of natural myocardial tissue, which bridged the electrically insulated structure of the matrix and promoted the propagation of electrical signals between the CMs and led to synchronized contraction. We hypothesized that Cig/(TA-Cu) scaffold loaded CMs could be taken as CP for MI repair, which might potentially replenish the lost CMs, bridge the electrical conduction between scar tissue and healthy

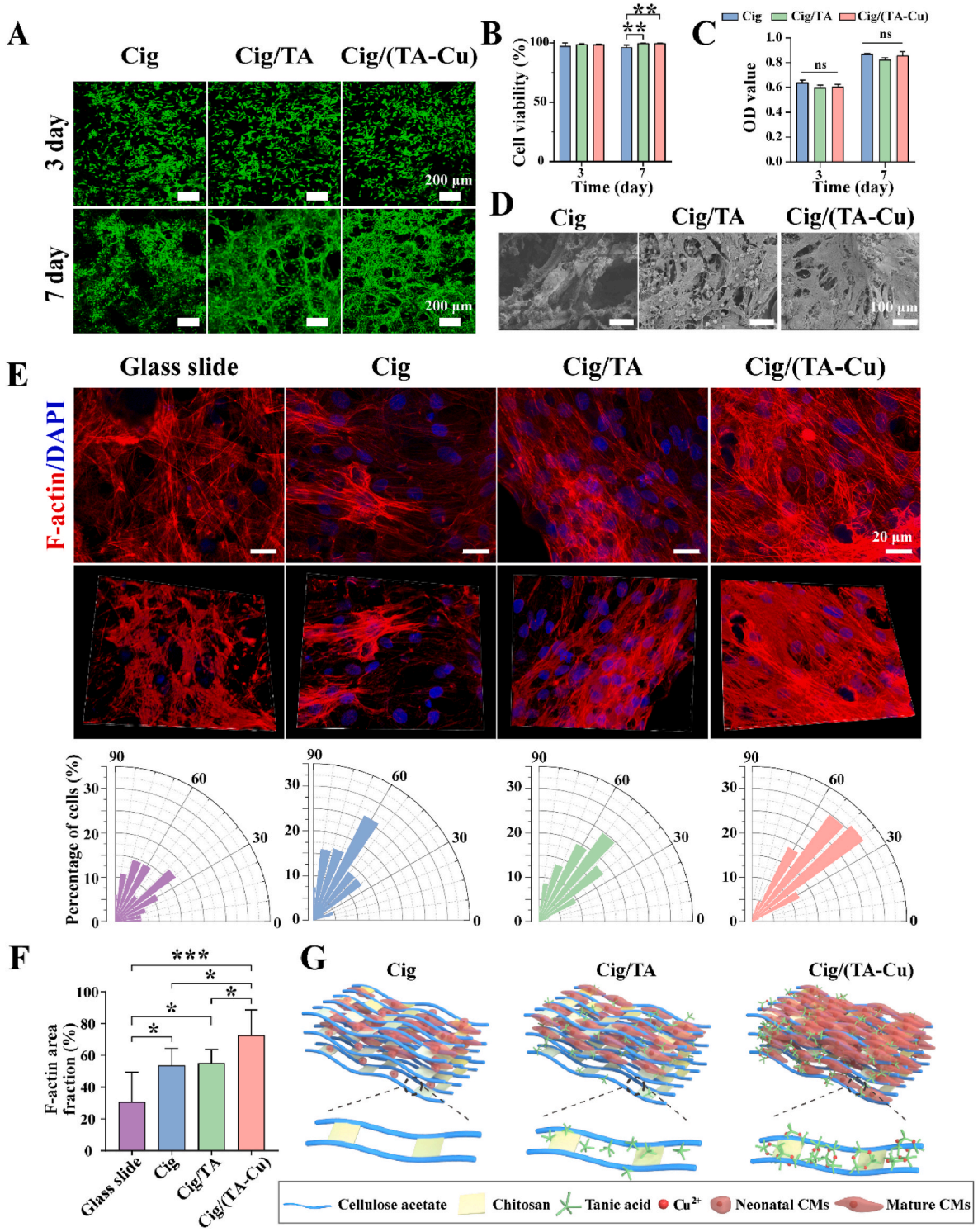

Fig. 2. The growth and alignment of CMs on the Cig/(TA-Cu) scaffold. (A) Live/dead staining of CMs cultured on different scaffolds for 3 days and 7 days. (B) Quantitative cell viability calculated by the ratio of the number of viable cells to the total cell population using live/dead staining (n = 4). (C) OD values measured by CCK-8 (n = 4). (D) SEM images of CMs cultured on Cig, Cig/TA, and Cig/(TA-Cu) scaffolds for 7 days. (E) F-actin staining for CMs on different scaffolds at day 7 (up: representative images shown in 2D pattern, middle: representative images shown in 3D pattern, bottom: polar graph analyses of orientation distribution about CMs cultured on different substrates). (F) Quantified cell spreading area from F-actin fluorescent staining (n = 4). *p < 0.05; **p < 0.01; ***p < 0.001. (G)The schematic illustrated the impacts of different scaffolds on the growth and orientation of CMs.

myocardium, and foster synchronous cardiac beating after MI.

3.4. Biomimetic Cig/(TA-Cu) scaffold alleviated oxidant stress damage in vitro

Typically, a burst of ROS occurs in the myocardium and induces severe oxidative stress damage to CMs after MI, ultimately leading to

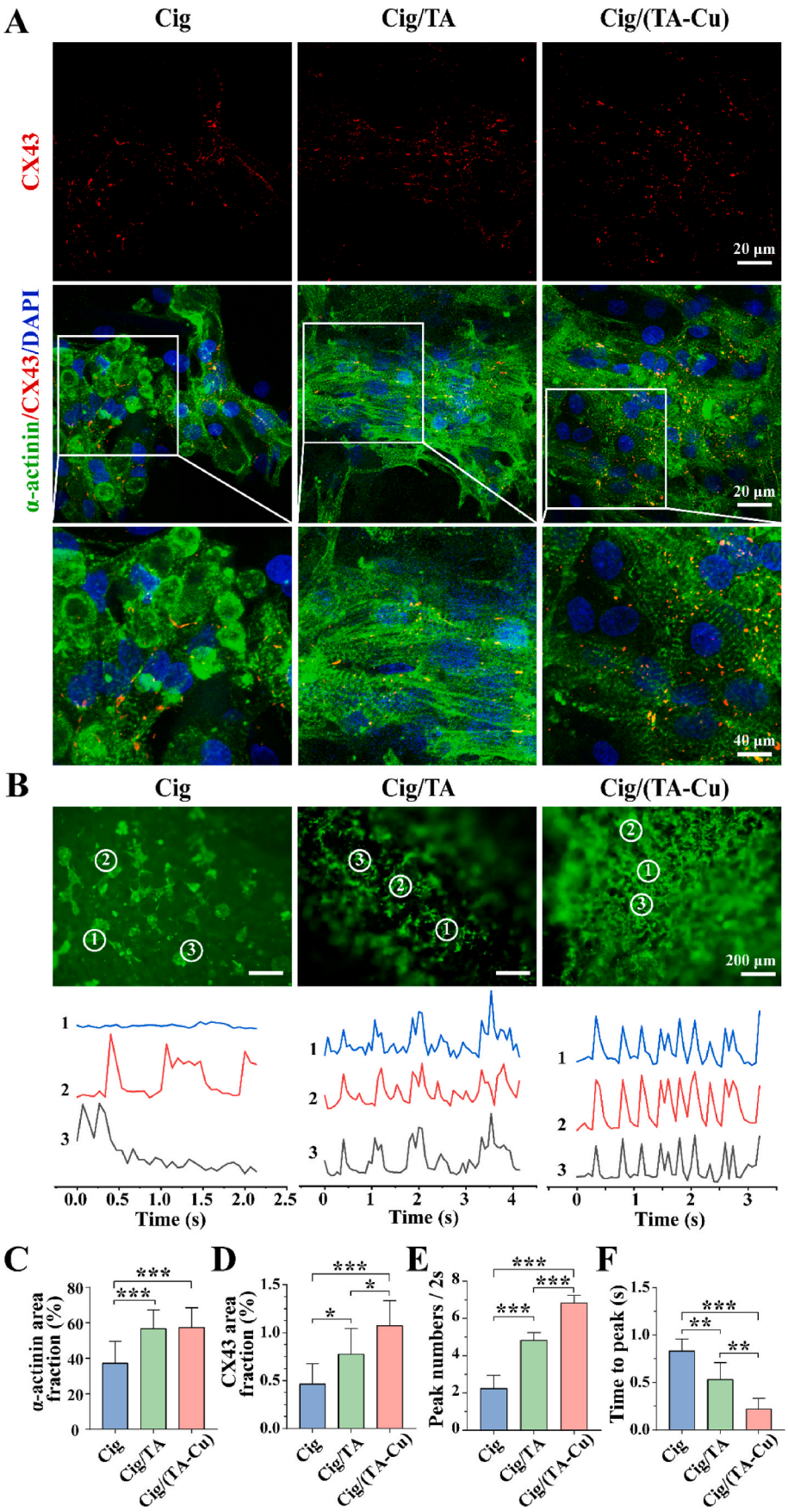

(caption on next page)

Fig. 3. Effect of the Cig/(TA-Cu) scaffold on CMs maturation and functionalization. (A) Immunofluorescence staining of α-actinin (green) and CX43 (red) of CMs on different scaffolds at day 7. (B) Calcium transient (up) and corresponding Ca^{2+} frequency signals (bottom) in CMs on different scaffolds at day 5. (C–D) Quantification for the expression of α-actinin (C) and CX43 (D) proteins in CMs on different scaffolds (n = 8). (E–F) Quantitative Ca^{2+} signal peak numbers were calculated every 2 s (E) and propagation time to Ca^{2+} signal peak (F) based on the images of (B) (n = 6). *p < 0.05; **p < 0.01; ***p < 0.001.

cardiac fibrosis and contractile dysfunction [64]. In this study, the antioxidant capacities of the scaffolds were evaluated in terms of the radical scavenging capability and specific scavenging activities ($O_2^{\bullet-}$, H_2O_2, and •OH). The antioxidant activity was first investigated by DPPH radical scavenging assay after DPPH solution was incubated with different scaffolds for 1.5 h (Fig. 4A, Fig. S12A). The purple color of DPPH solution faded quickly, and the UV–vis spectra showed the intensity of DPPH absorption peak at 517 nm was significantly declined in the Cig/TA and Cig/(TA-Cu) scaffolds compared to the Cig scaffold, manifesting that both Cig/TA and Cig/(TA-Cu) scaffolds could efficiently scavenge DPPH. Subsequently, NBT method was conducted to evaluate the inhibitory impact of various scaffolds on $O_2^{\bullet-}$. After NBT reaction solution incubated with the scaffolds for 20 min, a discernible lightning of the solution color was observed compared to the positive control group (Fig. S12B). The quantitative analysis showed that scavenging efficiency against $O_2^{\bullet-}$ in the Cig/(TA-Cu) scaffold was dramatically increased compared to the Cig scaffold, indicating that the Cig/(TA-Cu) scaffold could efficiently inhibit $O_2^{\bullet-}$ (Fig. 4B). Additionally, the scavenging capabilities of the scaffolds against H_2O_2 and •OH were investigated through H_2O_2/Ti $(SO_4)_2$ and Fe^{2+}/H_2O_2/Salicylic acid reaction system, respectively. The results showed that the Cig/(TA-Cu) scaffold could also decompose H_2O_2 and inhibit •OH (Fig. 4C and D).

Furthermore, we evaluated the cellular antioxidant capacity of the scaffolds by a H_2O_2-induced oxidative stress cell model. After H9C2 cells injured by 600 μM H_2O_2 were incubated with different scaffolds for 4 h, intracellular ROS and $O_2^{\bullet-}$ levels were measured by DCFH-DA and DHE fluorescent probes respectively. As shown in Fig. 4E–G, intense green (DCFH-DA) and red (DHE) fluorescence was detected in the pure H_2O_2 treatment group whereas substantially decreased fluorescence appeared in the Cig, Cig/TA and Cig/(TA-Cu) scaffolds. Statistical analysis demonstrated that the cells treated with Cig/(TA-Cu) scaffold exhibited the weakest fluorescence, indicating that the Cig/(TA-Cu) scaffold could potently attenuate the generation of intracellular ROS.

In summary, the Cig/(TA-Cu) scaffold exerted superior antioxidant effects as a robust scavenger of free radicals including $O_2^{\bullet-}$, H_2O_2, and •OH (Fig. 4H), which could be attributed to the electron transfer and hydrogen atom donated from TA-chelated Cu^{2+} functionalized platform on the scaffold [38]. The Cig/(TA-Cu) scaffold had the potential to rectify the deleterious ROS microenvironment and promote residence of CMs after implantation.

3.5. Biomimetic scaffold Cig/(TA-Cu) promoted angiogenesis in vitro

The effects of the scaffolds on angiogenesis were investigated through proliferation assay, scratch assay and tube formation assay. After HUVECs were cultured on different scaffolds for 1 day, substantial number of viable cells were attached to the scaffolds in the Cig/TA and Cig/(TA-Cu) group (Fig. 5A), suggesting good biocompatibility for HUVECs. Fig. 5B showed that HUVECs exhibited more commendable proliferation on the Cig/(TA-Cu) scaffold compared to the Cig and Cig/TA scaffolds. The cell migration was assessed after HUVECs cocultured with different scaffolds for 12 and 24 h. The results revealed that the most significant cell migration occurred in the Cig/(TA-Cu) group at 12 h and 24 h (Fig. 5C, D, and F). HUVECs tube formation assay was conducted to further assess the angiogenic potential of various scaffolds *in vitro*. After HUVECs were seeded on Matrigel and incubated with the scaffolds for 5 h, various degrees of honeycomb-like tubular structures were formed in different groups (Fig. 5E). Statistical analysis showed that the number of meshes (Fig. 5G) and the tube lengths (Fig. 5H) were significantly elevated in the Cig/(TA-Cu) group compared with other groups, indicating Cig/(TA-Cu) scaffold greatly enhanced tube formation of endothelial cells. These results could be ascribed to the Cu^{2+} from TA-chelated Cu^{2+} functionalized platform on the scaffold, which played role in promoting endothelial cell proliferation, migration and angiogenesis.

3.6. Biomimetic Cig/(TA-Cu) CP implantation scavenged ROS and reduced CMs apoptosis in the infarcted area

Motivated by the favorable *in vitro* outcomes, we adopted the scaffolds loaded CMs as biomimetic CPs which were implanted onto infarcted hearts. In detail, rats MI models were established by ligating the LAD and the rats were then treated in the following groups: pure CMs injection and CP implantation (Cig CP, Cig/TA CP, and Cig/(TA-Cu) CP). The Sham group underwent thoracotomy without LAD ligation. As illustrated in Fig. 6A, the effect of different CPs on antioxidant and antiapoptotic performance was evaluated after implantation for 3 days. Serum cTnT has been extensively used to assess the degree of ischemic myocardial injury [42]. The results showed that serum cTnT levels substantially increased after MI, which represented a severe myocardial damage and successful establishment of MI model. The implantation of the Cig/TA and Cig/(TA-Cu) CP significantly reduced myocardial injury compared to the MI group and pure CMs injection group (Fig. 6B). Next, DCFH-DA and DHE staining for cardiac section was utilized to visualize the intracellular ROS and $O_2^{\bullet-}$ at the infarcted area, respectively. Intense DCFH-DA and DHE fluorescence signal was observed in the MI group and pure CMs injection group, indicating substantial ROS was accumulated in the infarcted region. In contrast, fluorescence of DCFH-DA and DHE decreased significantly after CPs (especially Cig/(TA-Cu) CP) implantation compared to the MI group and pure CMs injection group at day 3 (Fig. 6C, D, G and I). The relative content of DHE in fresh heart tissue samples was determined by Tissue ROS detection kit (DHE). The results showed that DHE content was significantly decreased after CPs implantation (Fig. 6H), which was consistent with the results of fluorescence staining of cardiac section. Furthermore, the activities of SOD and GSH, and the content of MDA in cardiac tissue were measured respectively to assess oxidative stress levels. The SOD (an antioxidant enzyme) and GSH (an antioxidant) played pivotal roles in countering oxidative stress, which could clear free radical and shield cells from hyperoxia-induced damage, while MDA (a byproduct of lipid peroxidation) could reflect the severity of oxidative stress [65]. As shown in Fig. S14, the activities of SOD and GSH were markedly increased while the MDA content was substantially decreased in the Cig/(TA-Cu) CP group compared with the MI group.

Subsequently, the apoptosis of CMs at the infarcted area was assessed by TUNEL staining after 3 days of CPs implantation. The cell apoptosis rate was significantly diminished in the Cig/(TA-Cu) group compared to the MI group and pure CMs injection group (Fig. 6E and J), indicating the Cig/(TA-Cu) CP implantation effectively inhibited the CMs apoptosis. Moreover, immunofluorescence staining of cardiac sections showed that α-actinin protein expression was significantly diminished in the MI group compared to the Sham group whereas was upregulated in the Cig/(TA-Cu) CP group (Fig. 6F and K). These results confirmed that Cig/(TA-Cu) CP could protect CMs from oxidative stress damage by eliminating ROS during the early stages of MI, thereby reducing the CMs apoptosis in the infarction area and promoting the recovery of myocardial function.

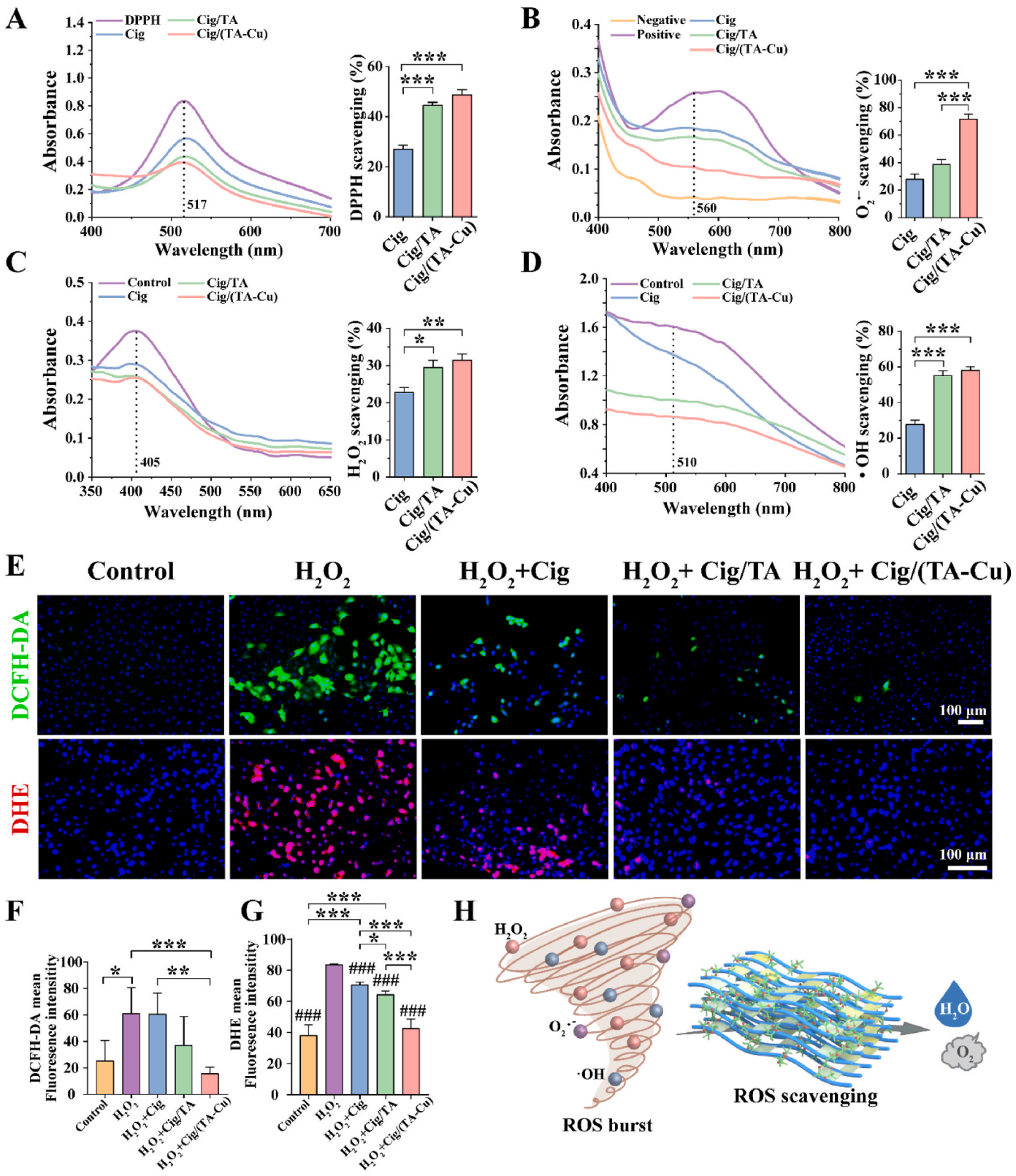

Fig. 4. Anti-oxidation capacity of the Cig/(TA-Cu) scaffold. (A–D) UV–vis spectra and scavenging percentage of DPPH radical (A), $O_2^{\bullet-}$ (B), H_2O_2 (C) and •OH (D) in the reaction solution after incubated with different scaffolds (n = 4). (E) Representative fluorescent images of ROS (DCFH-DA, green) and $O_2^{\bullet-}$ (DHE, red) in H9C2 cells injured by 600 μM H_2O_2 after cocultured with different scaffolds for 4 h. (F–G) Quantitative analysis of DCFH-DA fluorescence intensity (F) (n = 3) and DHE fluorescence intensity (G) (n = 8). ###p < 0.001 vs pure H_2O_2 group. *, **, and *** represent p < 0.05, p < 0.01, and p < 0.001 between the selected groups. (H) Schematic illustrated the antioxidation process of the Cig/(TA-Cu) scaffold.

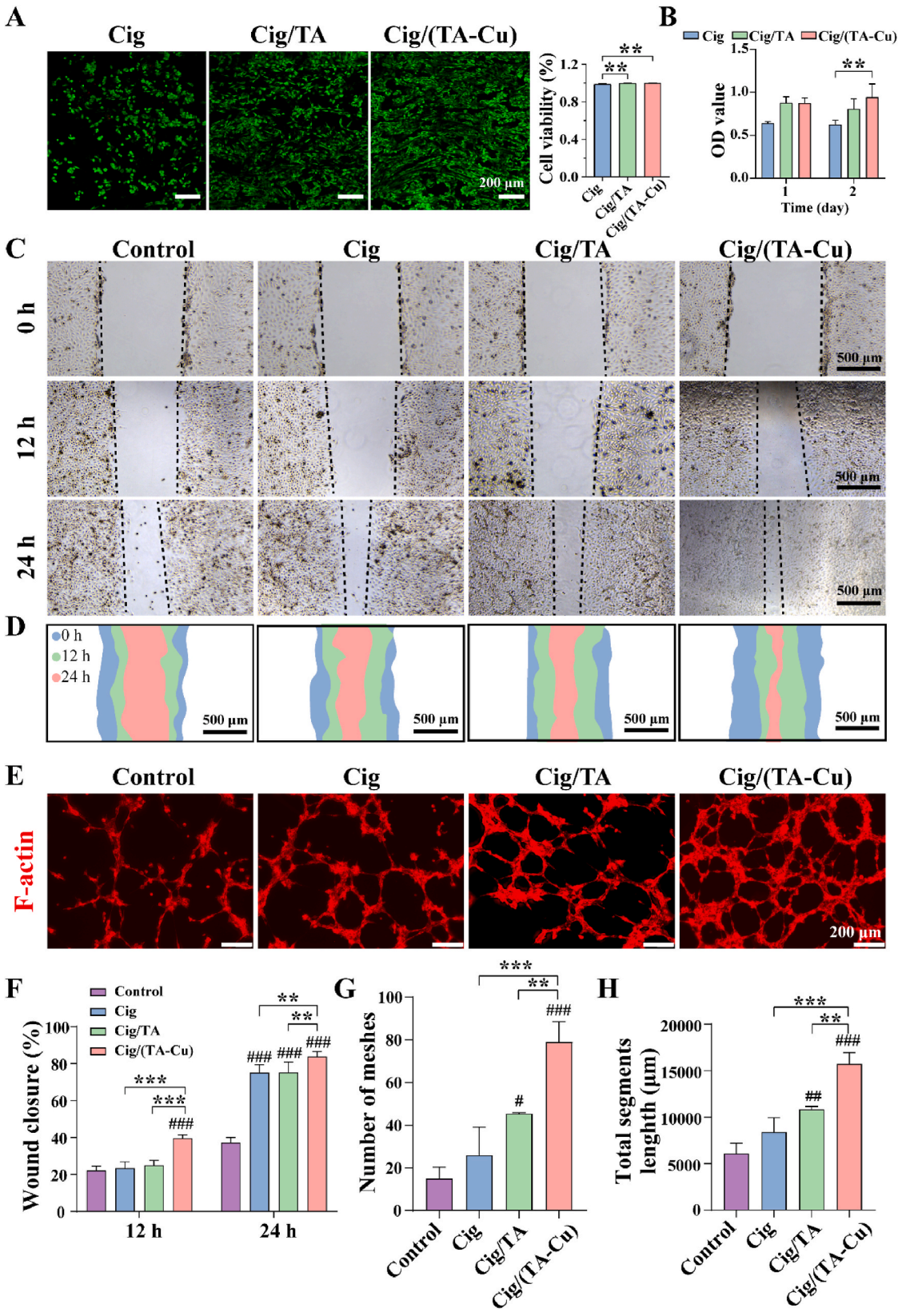

Fig. 5. *In vitro* pro-angiogenic effect of the Cig/(TA-Cu) scaffold. (A) Live/dead staining (left) and quantitative cell viability (right) of HUVECs cultured on Cig, Cig/TA, and Cig/(TA-Cu) scaffolds at day 1 (n = 5). (B) CCK-8 assay for HUVECs treated with different scaffolds for 1 day and 2 days (n = 4). (C–D) Representative scratch images (C) and closure trajectory diagrams (D) of HUVECs in different groups at 0, 12, and 24 h. (E) The F-actin staining of HUVECs on Matrigel in different groups after treatment for 5 h. (F) Cell migration quantification of HUVECs based on the images of (C) (n = 6). (G–H) Number of meshes (G) and total segments length (H) of tubular network were calculated based on the images of (E) (n = 3). #p < 0.05, ##p < 0.01, ###p < 0.001 vs the Control group. ** and *** represent p < 0.01 and p < 0.001 between the selected groups.

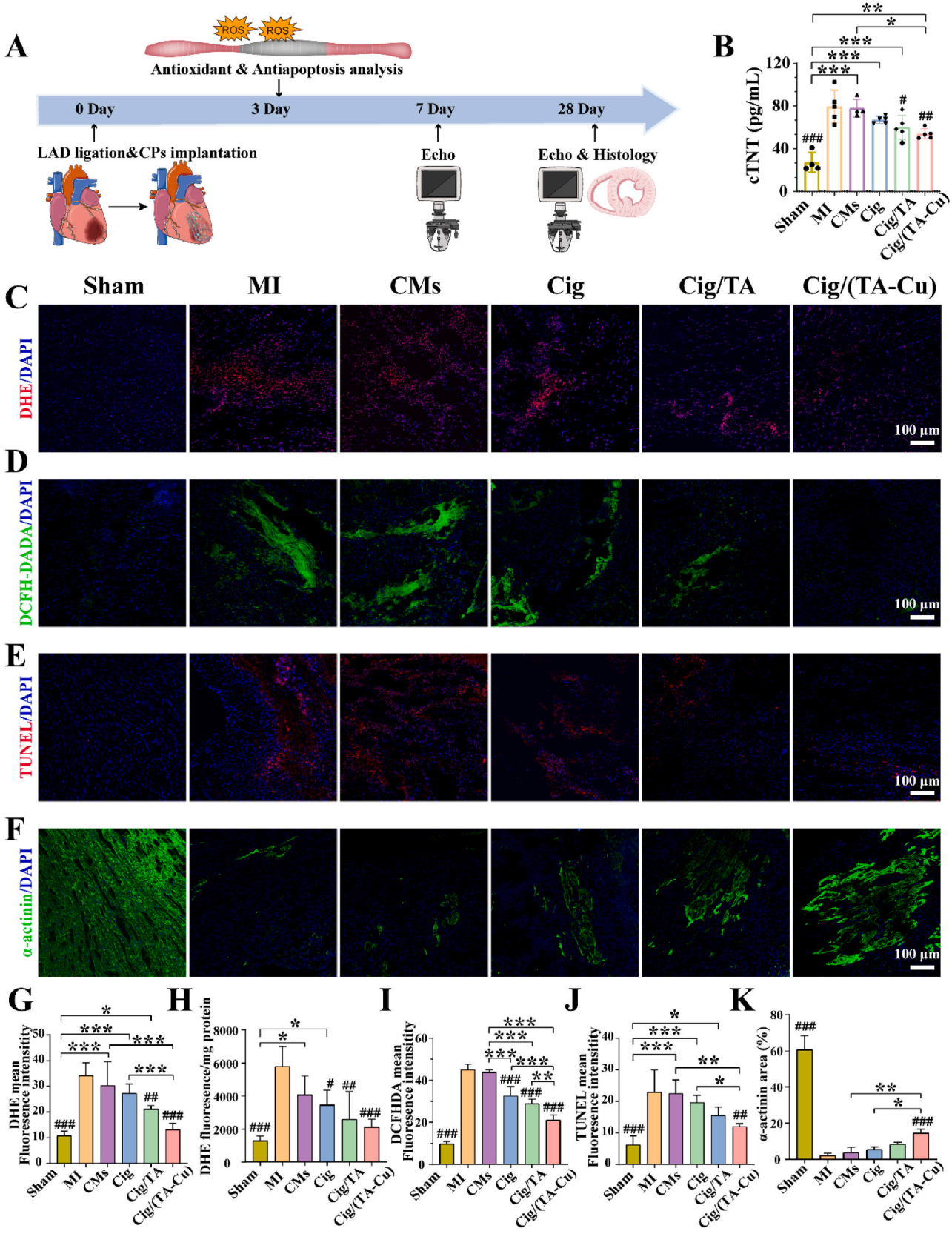

Fig. 6. Evaluation of ROS-scavenging and anti-apoptosis in the infarcted myocardium after Cig/(TA-Cu) CP implantation for 3 days. (A) Critical time points of animal experiments. (B) Rats serum cTnT levels in different groups were measured by ELISA after 3 days of surgery. (C–F) Representative staining images of DHE (C), DCFH-DA (D), TUNEL (E), and α-actinin (F) for heart sections in different groups at the infarcted site at day 3. (G) Quantitative analysis of DHE according to fluorescent images from (C) (n = 4). (H) Measurement of ROS levels in infarcted hearts by ROS detection kit (DHE) after different CPs implantation for 3 days (n = 4). (I–K) Quantitative analysis of DCFH-DA (I), TUNEL (J), and α-actinin (K) in different groups based on fluorescent staining images (n = 4). #p < 0.05, ##p < 0.01, ###p < 0.001 vs MI group. *, **, and *** represent p < 0.05, p < 0.01, and p < 0.001 between the selected groups.

3.7. Biomimetic Cig/(TA-Cu) CP implantation promoted cardiac electrical conduction after MI

Our previous studies suggested that conductive CPs could act as a robust tool to improve the electrical integration in the infarcted hearts, which was essential for the MI repair [26,62]. Here, we directly evaluated the influence of different CPs on electrical integration by measuring the electrical conduction velocities and local potential amplitudes between healthy and infarcted cardiac tissues within isolated Langendorff-perfused hearts after surgery for 28 days using an electrical mapping system. Representative activation maps for each group were recorded under electrical stimulation at 5 Hz and 4 V (Fig. 7A). The electrical conduction in the infarcted area was significantly delayed in the MI group and the pure CMs injection group, while the implantation of Cig CP, Cig/TA CP and Cig/(TA-Cu) CP accelerated the electrical propagation from the healthy myocardium to the infarcted region. The quantitative analysis showed that the highest conduction velocities occurred in the Cig/(TA-Cu) group, indicating that Cig/(TA-Cu) CP could dramatically promote the electrical conduction in the infarcted heart (Fig. 7D). Spontaneous local field potential in each group was recorded without external electrical stimulation, which demonstrated that the implantation of Cig/(TA-Cu) CP also significantly improved the local potential amplitude (Fig. 7B and E).

Furthermore, the level of electrical integration was assessed by detecting CX43 protein (an electron coupling protein) expression in the infarcted region after different CPs implantation. As shown in Fig. 7C, CX43 proteins in the infarcted areas were sparse in the MI group and the pure CMs injection group whereas were abundant in the Cig/(TA-Cu) group. Meanwhile, α-actinin positive myocardial tissues were plentiful and organized in the infarcted area of the Cig/(TA-Cu) group, which were densely dotted with CX43 proteins (Fig. 7C). Quantitative analysis showed that the positive area of α-actinin and CX43 proteins in the Cig/(TA-Cu) group were markedly upgraded than those in the MI group and the pure CMs injection group, reflecting a better electric-contraction at the tissue level (Fig. 7F and G). These results indicated that Cig/(TA-Cu) CP facilitated cardiac electrical integration at the infarcted area attributed to the improved expression of CX43 between CMs, which was caused by reducing CMs apoptosis and promoting the preservation of myocardial tissues.

3.8. Biomimetic Cig/(TA-Cu) CP implantation promoted myocardial repair in the infarcted heart

The effects of CPs on MI repair were investigated by echocardiography, histological analysis and immunofluorescent staining after implantation for 28 days. The echocardiograph images showed weak and rigid LV anterior wall contraction in the MI group and the pure CMs injection group, while stronger LV anterior wall contractile activity after CPs implantation. Interestingly, pronounced contractile waves of the LV anterior wall were detected in the Cig/(TA-Cu) group (Fig. 8A). Representative echocardiographic parameters including EF, FS, LVIDd, and LVIDs were further analyzed (Fig. 8B and C). Both EF and FS were dramatically declined in the MI group and the pure CMs injection group reflecting deteriorated cardiac systolic function, while were significantly elevated after CPs implantation, and the highest ΔEF% and ΔFS% occurred in the Cig/(TA-Cu) group. In addition, the values of LVIDs and LVIDd were substantially diminished only in the Cig/(TA-Cu) group. These results suggested that Cig/(TA-Cu) CP could improve the systolic function and suppress LV dilatation of infarcted hearts.

After CPs implantation for 28 days, less ventricle dilation and thicker ventricle wall were observed in the hearts of the Cig/TA CP and Cig/(TA-Cu) CP groups compared to the MI group and the pure CMs injection group under gross heart observation (Fig. S17). Furthermore, the pathological changes of cardiac structure were analyzed by Masson's trichrome staining. The results displayed that majority of the LV anterior wall was filled with fibrous tissue (blue) and bare myocardium tissues (red) in the MI group, while decreased fibrous tissues were observed in the Cig/TA CP and Cig/(TA-Cu) CP group (Fig. 8D). Quantitative analysis showed that both Cig/TA CP and Cig/(TA-Cu) CP implantation decreased the infarction area and elevated ventricle wall thickness, and Cig/(TA-Cu) CP group exhibited the smallest infarction area and largest ventricle wall thickness (Fig. 8H and I). Next, to analyze the effect of CPs on cardiac hypertrophy after implantation for 28 days, we visualized CMs by cTnT (a cardiac-specific protein) staining and marked CM boundaries using WGA (labeling glycoproteins of CM membrane) staining (Fig. 8E). The CM size was dramatically increased in the MI group and the pure CMs injection group compared to the Sham group, suggesting obvious ventricular hypertrophy. In contrast, the CM size was substantially reduced after CPs implantation, and the smallest size appeared in the Cig/(TA-Cu) group (Fig. 8J), manifesting that Cig/(TA-Cu) CP could significantly suppress CMs hypertrophy and reduce ventricular remodeling [66].

Effective myocardial repair after MI typically requires vigorous revascularization, which provides sufficient nutrition for the CMs, salvages the ischemic myocardium, and restore cardiac function [67,68]. Here, angiogenesis within the infarcted area was detected through immunofluorescent staining for cardiac sections using microvessels (vWF) and arterioles (vWF and α-SMA) markers. As shown in Fig. 8F, microvessels (vWF^+) and the arterioles (vWF^+/α-SMA^+) were substantially more abundant in the Cig/TA and Cig/(TA-Cu) groups than in other groups. Quantitative analysis showed that the number of vessels in the Cig/(TA-Cu) group was significantly higher than that in the MI group (Fig. 8K), indicating that the Cig/(TA-Cu) CP could substantially promote angiogenesis. Previous studies have shown that macrophages which extensively infiltrate the infarcted myocardium also involve in this angiogenesis process for cardiac repair. Inflammatory M1 macrophages could aggravate tissue damage whereas M2 macrophages could secrete massive cytokines to promote angiogenesis [69,70]. Therefore, we conducted immunofluorescent staining of heart sections to assess the population of M2 and M1 macrophages by CD206 (red) and CD86 (green) marker, respectively (Fig. 8G). After CPs implantation for 28 days, extensive infiltration of pro-inflammatory M1 macrophages and sparse reparative M2 macrophages were observed in the MI group, while the M2/M1 ratio was significantly increased in the Cig/TA and Cig/(TA-Cu) groups (Fig. 8L), which was consistent with the angiogenesis process. Taken together, these results suggested that Cig/(TA-Cu) CP could improve the cardiac function, suppress LV remodeling and promote vascular regeneration. Compared to the previous materials (such as decellularized extracellular matrix bioinks, conductive biomaterials and anisotropic fibers) related to the ECM niche in MI repair [21,71–73], our CP integrates multimodal cues into one system, thus creating a more biomimetic cardiac ECM niche that is more conducive to MI repair.

4. Conclusions

In conclusion, we successfully tailored the waste cigarette filter into a functional Cig/(TA-Cu) CP served as biomimetic cardiac niche for MI repair. The simple surface-modification of structural anisotropic cigarette filter with TA-Cu complex endows the Cig/(TA-Cu) CP with well-aligned fiber microstructures, electrical conductivity and mechanical properties resembling natural myocardium, which was conceive to growth, orientation, maturation, and functionalization of CMs. This CP could significantly inhibit the ROS burst, reduce CM apoptosis, enhance synchronous contraction of CMs, foster endothelial cells angiogenesis to reverse the aberrant microenvironment, thereby facilitating myocardial electrical integration, promoting vascular regeneration, and improving cardiac function. Our results demonstrated that cigarette filters with the consistent orientation structure from the interior to the exterior potentially provide a controllable, reproducible and low-cost approach to construct an anisotropic CP.

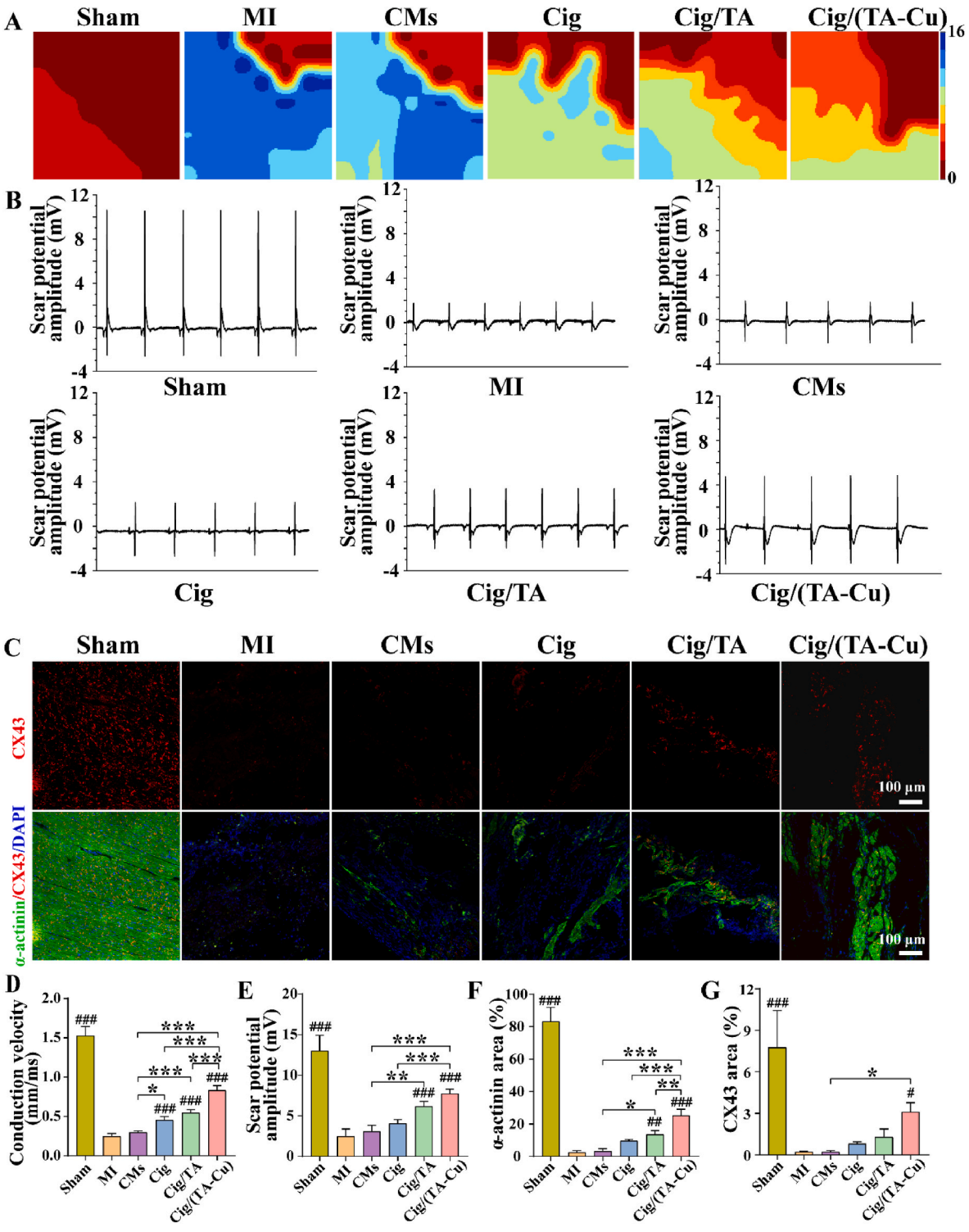

Fig. 7. Reconstruction of electrical conduction in the infarcted myocardium after Cig/(TA-Cu) CP implantation for 28 days. (A) Representative epicardial activation maps were recorded by 64-channel electromapping system from the healthy myocardium to the infarcted myocardium in different groups. Ruler: red represented the first activation, blue represented the last activation; and numbers indicated activation time (ms). The conduction direction arrived from red to blue. (B) The spontaneous potential amplitudes at the infarcted area in different groups without additional stimulation. (C) Immunofluorescence staining of cardiac-specific proteins (α-actinin: green, CX43: red) in the infarcted area after CPs implantation. (D) Conduction velocities in different groups were calculated according to epicardial activation maps (n = 4). (E) The average potential amplitudes were obtained based on the images of (B) (n = 4). (F–G) Quantitative analysis of α-actinin (F) and CX43 (G) positive area in different groups (n = 4). #$p < 0.05$, ##$p < 0.01$, ###$p < 0.001$ vs MI group. *, **, and *** represent $p < 0.05$, $p < 0.01$, and $p < 0.001$ between the selected groups.

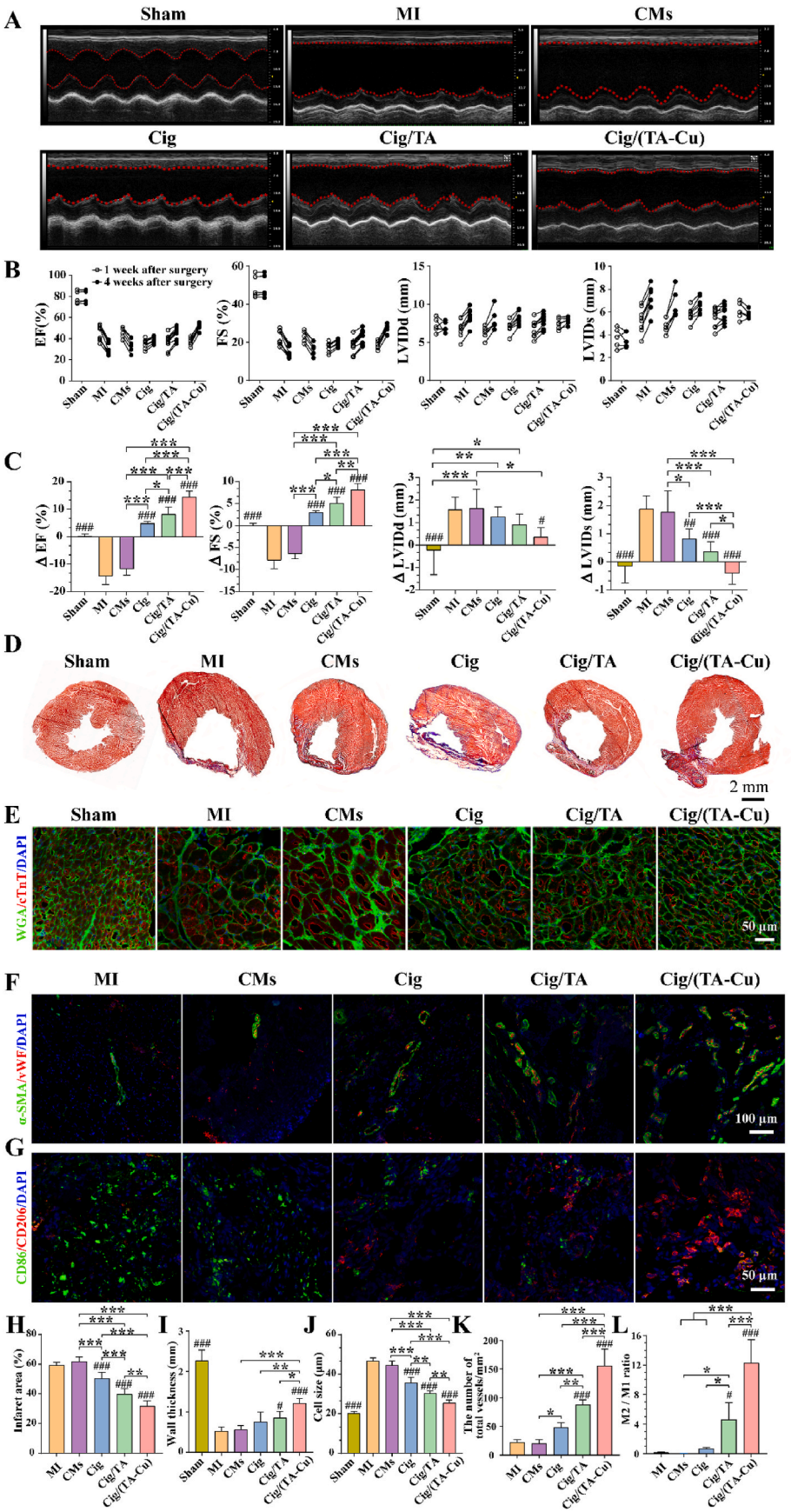

(caption on next page)

Fig. 8. Repair effects of Cig/(TA-Cu) CP in rat MI models after implantation for 28 days. (A) Representative echocardiographic images (M-mode) of rat hearts in all groups after CPs implantation for 28 days. (B) FS, EF, LVIDs, and LVIDd in different groups were determined by echocardiography at day 7 and day 28 after implantation. (C) Statistical analysis of the changes of FS, EF, LVIDs, and LVIDd in different groups after CPs implantation for 28 days (n = 6). (D) Masson's trichrome staining of cardiac sections in different groups showed the fibrous tissue (blue) and myocardium (red). (E) Immunofluorescence staining of WGA (green) and cTnT (red) to display the boundaries of CMs within the border area. (F–G) Immunofluorescence staining of α-SMA (green)/vWF (red) (F), and CD86 (green)/CD206 (red) (G) within the infarcted area in different groups. (H–I) Quantitative analysis of infarct area (H) and wall thickness (I) of LV anterior wall in different groups based on the Masson' s trichrome staining images (n = 6). (J–L) Statistical analysis of CM size (J) (n = 4), microvessel densities (K) (n = 5), and the ratio of M2/M1 macrophages (L) (n = 4) within the infarcted region in different groups based on WGA, vWF/α-SMA, and CD86/CD206 staining, respectively. #p < 0.05, ##p < 0.01, ###p < 0.001 vs MI group. *, **, and *** represent p < 0.05, p < 0.01, and p < 0.001 between the selected groups.

Ethics approval

Experimental and animal care procedures were approved by the Southern Medical University Ethics Committee (SYXK(Guangdong) 2021-0167).

CRediT authorship contribution statement

Guofeng Tang: Writing – review & editing, Writing – original draft, Visualization, Validation, Software, Resources, Methodology, Investigation, Formal analysis, Data curation, Conceptualization. **Zhentao Li:** Writing – review & editing, Visualization, Validation, Software, Project administration, Methodology, Investigation, Funding acquisition, Formal analysis, Data curation, Conceptualization. **Chengbin Ding:** Visualization, Validation, Methodology, Investigation, Formal analysis, Data curation, Conceptualization. **Jiang Zhao:** Investigation, Data curation, Formal analysis, Validation, Visualization. **Xianglong Xing:** Visualization, Validation, Investigation, Formal analysis, Data curation. **Yan Sun:** Visualization, Validation, Software, Investigation, Formal analysis, Data curation. **Xiaozhong Qiu:** Writing – review & editing, Supervision, Resources, Project administration, Methodology, Funding acquisition, Conceptualization. **Leyu Wang:** Writing – review & editing, Supervision, Project administration, Methodology, Funding acquisition, Conceptualization.

Declaration of competing interest

The authors declare that they have no competing interests.

Acknowledgments

This work was supported by the National Natural Science Foundation of China (Grant No. 32071355, U21A20173, 32071363, 32201083), the National Key R&D program of China (2023YFC2412803, 2022YFC2402801), Science and Technology Planning Project of Guangdong Province (2022A1515011888), and the Marine Economy Development Project of Department of Natural Resources of Guangdong Province (No. GDNRC[2022]039), China Postdoctoral Fund Program (No. 2021M701599), and Shenzhen Fundamental Research Key Project (JCYJ20200109150641992).

Appendix A. Supplementary data

Supplementary data to this article can be found online at https://doi.org/10.1016/j.bioactmat.2024.02.012.

References

[1] G.W. Reed, J.E. Rossi, C.P. Cannon, Acute myocardial infarction, Lancet (London, England) 389 (10065) (2017) 197–210, https://doi.org/10.1016/s0140-6736(16)30677-8.

[2] M.D. Samsky, D.A. Morrow, A.G. Proudfoot, J.S. Hochman, H. Thiele, S.V. Rao, Cardiogenic shock after acute myocardial infarction: a review, JAMA 326 (18) (2021) 1840–1850, https://doi.org/10.1001/jama.2021.18323.

[3] S.P. Kwon, B.H. Hwang, E.H. Park, H.Y. Kim, J.R. Lee, M. Kang, S.Y. Song, M. Jung, H.S. Sohn, E. Kim, C.W. Kim, K.Y. Lee, G.C. Oh, E. Choo, S. Lim, Y. Chung, K. Chang, B.S. Kim, Nanoparticle-Mediated blocking of excessive inflammation for prevention of heart failure following myocardial infarction, Small 17 (32) (2021) e2101207, https://doi.org/10.1002/smll.202101207.

[4] T. Wu, X. Zhang, Y. Liu, C. Cui, Y. Sun, W. Liu, Wet adhesive hydrogel cardiac patch loaded with anti-oxidative, autophagy-regulating molecule capsules and MSCs for restoring infarcted myocardium, Bioact. Mater. 21 (2023) 20–31, https://doi.org/10.1016/j.bioactmat.2022.07.029.

[5] K. Ashtari, H. Nazari, H. Ko, P. Tebon, M. Akhshik, M. Akbari, S.N. Alhosseini, M. Mozafari, B. Mehravi, M. Soleimani, R. Ardehali, M. Ebrahimi Warkiani, S. Ahadian, A. Khademhosseini, Electrically conductive nanomaterials for cardiac tissue engineering, Adv. Drug Deliv. Rev. 144 (2019) 162–179, https://doi.org/10.1016/j.addr.2019.06.001.

[6] H. Ryu, X. Wang, Z. Xie, J. Kim, Y. Liu, W. Bai, Z. Song, J.W. Song, Z. Zhao, J. Kim, Q. Yang, J.J. Xie, R. Keate, H. Wang, Y. Huang, I.R. Efimov, G.A. Ameer, J. A. Rogers, Materials and design approaches for a fully bioresorbable, electrically conductive and mechanically compliant cardiac patch Technology, Adv. Sci. 10 (27) (2023) e2303429, https://doi.org/10.1002/advs.202303429.

[7] C. Zhang, M.H. Hsieh, S.Y. Wu, S.H. Li, J. Wu, S.M. Liu, H.J. Wei, R.D. Weisel, H. W. Sung, R.K. Li, A self-doping conductive polymer hydrogel that can restore electrical impulse propagation at myocardial infarct to prevent cardiac arrhythmia and preserve ventricular function, Biomaterials 231 (2020) 119672, https://doi.org/10.1016/j.biomaterials.2019.119672.

[8] K. Klaourakis, J.M. Vieira, P.R. Riley, The evolving cardiac lymphatic vasculature in development, repair and regeneration, Nature reviews, Cardiology 18 (5) (2021) 368–379, https://doi.org/10.1038/s41569-020-00489-x.

[9] Y. Song, H. Wang, F. Yue, Q. Lv, B. Cai, N. Dong, Z. Wang, L. Wang, Silk-based biomaterials for cardiac tissue engineering, Adv. Healthcare Mater. (2020) e2000735, https://doi.org/10.1002/adhm.202000735.

[10] M.M. Kittleson, J.A. Kobashigawa, Cardiac transplantation: current outcomes and contemporary controversies, JACC, Heart Fail. 5 (12) (2017) 857–868, https://doi.org/10.1016/j.jchf.2017.08.021.

[11] R.D. Pedde, B. Mirani, A. Navaei, T. Styan, S. Wong, M. Mehrali, A. Thakur, N. K. Mohtaram, A. Bayati, A. Dolatshahi-Pirouz, M. Nikkhah, S.M. Willerth, M. Akbari, Emerging biofabrication strategies for engineering complex tissue constructs, Adv. Mater. 29 (19) (2017) 1606061, https://doi.org/10.1002/adma.201606061.

[12] L. He, X. Chen, Cardiomyocyte induction and regeneration for myocardial infarction treatment: cell sources and administration strategies, Adv. Healthcare Mater. 9 (22) (2020) e2001175, https://doi.org/10.1002/adhm.202001175.

[13] J. Zhang, R. Bolli, D.J. Garry, E. Marbán, P. Menasché, W.H. Zimmermann, T. J. Kamp, J.C. Wu, V.J. Dzau, Basic and translational Research in cardiac repair and regeneration: JACC state-of-the-art review, J. Am. Coll. Cardiol. 78 (21) (2021) 2092–2105, https://doi.org/10.1016/j.jacc.2021.09.019.

[14] K.D. Dwyer, K.L.K. Coulombe, Cardiac mechanostructure: using mechanics and anisotropy as inspiration for developing epicardial therapies in treating myocardial infarction, Bioact. Mater. 6 (7) (2021) 2198–2220, https://doi.org/10.1016/j.bioactmat.2020.12.015.

[15] H. Savoji, M.H. Mohammadi, N. Rafatian, M.K. Toroghi, E.Y. Wang, Y. Zhao, A. Korolj, S. Ahadian, M. Radisic, Cardiovascular disease models: a game changing paradigm in drug discovery and screening, Biomaterials 198 (2019) 3–26, https://doi.org/10.1016/j.biomaterials.2018.09.036.

[16] Y. Yao, A. Li, S. Wang, Y. Lu, J. Xie, H. Zhang, D. Zhang, J. Ding, Z. Wang, C. Tu, L. Shen, L. Zhuang, Y. Zhu, C. Gao, Multifunctional elastomer cardiac patches for preventing left ventricle remodeling after myocardial infarction in vivo, Biomaterials 282 (2022) 121382, https://doi.org/10.1016/j.biomaterials.2022.121382.

[17] S. Liang, Y. Zhang, H. Wang, Z. Xu, J. Chen, R. Bao, B. Tan, Y. Cui, G. Fan, W. Wang, W. Wang, W. Liu, Paintable and rapidly bondable conductive hydrogels as therapeutic cardiac patches, Adv. Mater. 30 (23) (2018) e1704235, https://doi.org/10.1002/adma.201704235.

[18] X. Song, J. Zhang, S. Shen, D. Liu, J. Zhang, W. Yin, G. Ye, L. Wang, L. Cai, H. Hou, X. Qiu, Cardiac-adaptive conductive hydrogel patch enabling construction of mechanical-electrical anisotropic microenvironment for heart repair, Research 6 (2023) 0161, https://doi.org/10.34133/research.0161.

[19] X. Wei, L. Wang, C. Duan, K. Chen, X. Li, X. Guo, P. Chen, H. Liu, Y. Fan, Cardiac patches made of brown adipose-derived stem cell sheets and conductive electrospun nanofibers restore infarcted heart for ischemic myocardial infarction, Bioact. Mater. 27 (2023) 271–287, https://doi.org/10.1016/j.bioactmat.2023.03.023.

[20] T. Hao, J. Li, F. Yao, D. Dong, Y. Wang, B. Yang, C. Wang, Injectable fullerenol/alginate hydrogel for suppression of oxidative stress damage in Brown adipose-derived stem cells and cardiac repair, ACS Nano 11 (6) (2017) 5474–5488, https://doi.org/10.1021/acsnano.7b00221.

[21] J. Zhan, X. Liao, X. Fan, J. Zhang, H. Li, Y. Cai, X. Qiu, An injectable and conductive TEMPOL/polypyrrole integrated peptide co-assembly hydrogel promotes functional maturation of cardiomyocytes for myocardial infarction repair, Compos. B Eng. 236 (2022) 109794, https://doi.org/10.1016/j.compositesb.2022.109794.

[22] G. Zhao, Y. Feng, L. Xue, M. Cui, Q. Zhang, F. Xu, N. Peng, Z. Jiang, D. Gao, X. Zhang, Anisotropic conductive reduced graphene oxide/silk matrices promote post-infarction myocardial function by restoring electrical integrity, Acta Biomater. 139 (2022) 190–203, https://doi.org/10.1016/j.actbio.2021.03.073.

[23] J. Feng, H. Shi, X. Yang, S. Xiao, Self-adhesion conductive sub-micron fiber cardiac patch from shape memory polymers to promote electrical signal transduction function, ACS Appl. Mater. Interfaces 13 (17) (2021) 19593–19602, https://doi.org/10.1021/acsami.0c22844.

[24] B.A. Tompkins, W. Balkan, J. Winkler, M. Gyöngyösi, G. Goliasch, F. Fernández-Avilés, J.M. Hare, Preclinical studies of stem cell therapy for heart disease, Circ. Res. 122 (7) (2018) 1006–1020, https://doi.org/10.1161/circresaha.117.312486.

[25] C. Fan, J. Shi, Y. Zhuang, L. Zhang, L. Huang, W. Yang, B. Chen, Y. Chen, Z. Xiao, H. Shen, Y. Zhao, J. Dai, Myocardial-infarction-responsive smart hydrogels targeting matrix metalloproteinase for on-demand growth factor delivery, Adv. Mater. 31 (40) (2019) e1902900, https://doi.org/10.1002/adma.201902900.

[26] L. Wang, Y. Liu, G. Ye, Y. He, B. Li, Y. Guan, B. Gong, K. Mequanint, M.M.Q. Xing, X. Qiu, Injectable and conductive cardiac patches repair infarcted myocardium in rats and minipigs, Nat. Biomed. Eng. 5 (10) (2021) 1157–1173, https://doi.org/10.1038/s41551-021-00796-9.

[27] Y. He, Q. Li, P. Chen, Q. Duan, J. Zhan, X. Cai, L. Wang, H. Hou, X. Qiu, A smart adhesive Janus hydrogel for non-invasive cardiac repair and tissue adhesion prevention, Nat. Commun. 13 (1) (2022) 7666, https://doi.org/10.1038/s41467-022-35437-5.

[28] M. Xing, Y. Jiang, W. Bi, L. Gao, Y.L. Zhou, S.L. Rao, L.L. Ma, Z.W. Zhang, H. T. Yang, J. Chang, Strontium ions protect hearts against myocardial ischemia/reperfusion injury, Sci. Adv. 7 (3) (2021) eabe0726, https://doi.org/10.1126/sciadv.abe0726.

[29] S. Liu, Z. Wang, X. Chen, M. Han, J. Xu, T. Li, L. Yu, M. Qin, M. Long, M. Li, H. Zhang, Y. Li, L. Wang, W. Huang, Y. Wu, Multiscale anisotropic scaffold integrating 3D printing and electrospinning techniques as a heart-on-a-chip platform for evaluating drug-induced cardiotoxicity, Adv. Healthcare Mater. 12 (24) (2023) e2300719, https://doi.org/10.1002/adhm.202300719.

[30] K. Metavarayuth, P. Sitasuwan, J.A. Luckanagul, S. Feng, Q. Wang, Virus nanoparticles mediated osteogenic differentiation of bone derived mesenchymal stem cells, Adv. Sci. 2 (10) (2015) 1500026, https://doi.org/10.1002/advs.201500026.

[31] H.S. Yang, B. Lee, J.H. Tsui, J. Macadangdang, S.Y. Jang, S.G. Im, D.H. Kim, Electroconductive nanopatterned substrates for enhanced myogenic differentiation and maturation, Adv. Healthcare Mater. 5 (1) (2016) 137–145, https://doi.org/10.1002/adhm.201500003.

[32] W. Xie, X. Wei, H. Kang, H. Jiang, Z. Chu, Y. Lin, Y. Hou, Q. Wei, Static and dynamic: evolving biomaterial mechanical properties to control cellular mechanotransduction, Adv. Sci. 10 (9) (2023) e2204594, https://doi.org/10.1002/advs.202204594.

[33] L. Tian, J. Yang, X. You, M. Wang, X. Ren, X. Zhang, S. Dong, Tailoring centripetal metamaterial with superelasticity and negative Poisson's ratio for organic solvents adsorption, Sci. Adv. 8 (39) (2022) eabo1014, https://doi.org/10.1126/sciadv.abo1014.

[34] F. Huang, Y. Xu, B. Peng, Y. Su, F. Jiang, Y.-L. Hsieh, Q. Wei, Coaxial electrospun cellulose-core fluoropolymer-shell fibrous membrane from recycled cigarette filter as separator for high performance lithium-ion battery, ACS Sustain. Chem. Eng. 3 (5) (2015) 932–940, https://doi.org/10.1021/acssuschemeng.5b00032.

[35] S. Roy, T. Das, B. Dasgupta Ghosh, K.L. Goh, K. Sharma, Y.W. Chang, From hazardous waste to green applications: selective surface functionalization of waste cigarette filters for high-performance robust triboelectric nanogenerators and CO (2) adsorbents, ACS Appl. Mater. Interfaces 14 (28) (2022) 31973–31985, https://doi.org/10.1021/acsami.2c06463.

[36] M.R. Khan, S. Liao, A. Farooq, M.A. Naeem, M. Wasim, Q. Wei, Regeneration and modification of cellulose acetate from cigarette waste: biomedical potential by encapsulation of tetracycline hydrochloride, Int. J. Biol. Macromol. 250 (2023) 126266, https://doi.org/10.1016/j.ijbiomac.2023.126266.

[37] H. Ejima, J.J. Richardson, K. Liang, J.P. Best, M.P. van Koeverden, G.K. Such, J. Cui, F. Caruso, One-step assembly of coordination complexes for versatile film and particle engineering, Science (New York, N.Y.) 341 (6142) (2013) 154–157, https://doi.org/10.1126/science.1237265.

[38] K. Wu, W. Hua, X. Li, J. Lin, Facile pH-responsive injectable polyphenol-europium assembly coordination complex with enhanced antioxidation and angiogenesis for myocardial infarction treatment, Chem. Eng. J. 446 (2022) 136835, https://doi.org/10.1016/j.cej.2022.136835.

[39] X. Li, P. Gao, J. Tan, K. Xiong, M.F. Maitz, C. Pan, H. Wu, Y. Chen, Z. Yang, N. Huang, Assembly of metal-phenolic/catecholamine networks for synergistically anti-inflammatory, antimicrobial, and anticoagulant coatings, ACS Appl. Mater. Interfaces 10 (47) (2018) 40844–40853, https://doi.org/10.1021/acsami.8b14409.

[40] Y. Li, Y. Miao, L. Yang, Y. Zhao, K. Wu, Z. Lu, Z. Hu, J. Guo, Recent advances in the development and antimicrobial applications of metal-phenolic networks, Adv. Sci. 9 (27) (2022) e2202684, https://doi.org/10.1002/advs.202202684.

[41] Y.N. Slavin, J. Asnis, U.O. Häfeli, H. Bach, Metal nanoparticles: understanding the mechanisms behind antibacterial activity, J. Nanobiotechnol. 15 (1) (2017) 1–20, https://doi.org/10.1186/s12951-017-0308-z.

[42] T. Hao, M. Qian, Y. Zhang, Q. Liu, A.C. Midgley, Y. Liu, Y. Che, J. Hou, Q. Zhao, An injectable dual-function hydrogel protects against myocardial ischemia/reperfusion injury by modulating ROS/NO disequilibrium, Adv. Sci. 9 (15) (2022) e2105408, https://doi.org/10.1002/advs.202105408.

[43] S. Li, L. Zhang, C. Liu, J. Kim, K. Su, T. Chen, L. Zhao, X. Lu, H. Zhang, Y. Cui, X. Cui, F. Yuan, H. Pan, Spontaneous immunomodulation and regulation of angiogenesis and osteogenesis by Sr/Cu-borosilicate glass (BSG) bone cement to repair critical bone defects, Bioact. Mater. 23 (2023) 101–117, https://doi.org/10.1016/j.bioactmat.2022.10.021.

[44] J. Zhang, H. Wu, F. He, T. Wu, L. Zhou, J. Ye, Concentration-dependent osteogenic and angiogenic biological performances of calcium phosphate cement modified with copper ions, Mater. Sci. Eng., C 99 (2019) 1199–1212, https://doi.org/10.1016/j.msec.2019.02.042.

[45] J. Sun, H. Guo, G.N. Schädli, K. Tu, S. Schär, F. Schwarze, G. Panzarasa, J. Ribera, I. Burgert, Enhanced mechanical energy conversion with selectively decayed wood, Sci. Adv. 7 (11) (2021) eabd9138, https://doi.org/10.1126/sciadv.abd9138.

[46] Y. Li, R. Fu, Z. Duan, C. Zhu, D. Fan, Adaptive hydrogels based on nanozyme with dual-enhanced triple enzyme-like activities for wound disinfection and mimicking antioxidant defense system, Adv. Healthcare Mater. 11 (2) (2022) e2101849, https://doi.org/10.1002/adhm.202101849.

[47] C. Song, X. Zhang, L. Wang, F. Wen, K. Xu, W. Xiong, C. Li, B. Li, Q. Wang, M.M. Q. Xing, X. Qiu, An injectable conductive three-dimensional elastic network by tangled surgical-suture spring for heart repair, ACS Nano 13 (12) (2019) 14122–14137, https://doi.org/10.1021/acsnano.9b06761.

[48] L. Wang, J. Jiang, W. Hua, A. Darabi, X. Song, C. Song, W. Zhong, M.M.Q. Xing, X. Qiu, Mussel-Inspired conductive cryogel as cardiac tissue patch to repair myocardial infarction by migration of conductive nanoparticles, Adv. Funct. Mater. 26 (24) (2016) 4293–4305, https://doi.org/10.1002/adfm.201505372.

[49] B.H. Morrow, G.F. Payne, J. Shen, pH-responsive self-assembly of polysaccharide through a rugged energy landscape, J. Am. Chem. Soc. 137 (40) (2015) 13024–13030, https://doi.org/10.1021/jacs.5b07761.

[50] L. Jiang, Z. Sun, X. Chen, J. Li, Y. Xu, Y. Zu, J. Hu, D. Han, C. Yang, Cells sensing mechanical cues: stiffness influences the lifetime of cell-extracellular matrix interactions by affecting the loading rate, ACS Nano 10 (1) (2016) 207–217, https://doi.org/10.1021/acsnano.5b03157.

[51] H. Li, B. Yu, P. Yang, J. Zhan, X. Fan, P. Chen, X. Liao, C. Ou, Y. Cai, M. Chen, Injectable AuNP-HA matrix with localized stiffness enhances the formation of gap junction in engrafted human induced pluripotent stem cell-derived cardiomyocytes and promotes cardiac repair, Biomaterials 279 (2021) 121231, https://doi.org/10.1016/j.biomaterials.2021.121231.

[52] G. Ye, Z. Wen, F. Wen, X. Song, L. Wang, C. Li, Y. He, S. Prakash, X. Qiu, Mussel-inspired conductive Ti(2)C-cryogel promotes functional maturation of cardiomyocytes and enhances repair of myocardial infarction, Theranostics 10 (5) (2020) 2047–2066, https://doi.org/10.7150/thno.38876.

[53] M. Kapnisi, C. Mansfield, C. Marijon, A.G. Guex, F. Perbellini, I. Bardi, E. J. Humphrey, J.L. Puetzer, D. Mawad, D.C. Koutsogeorgis, D.J. Stuckey, C. M. Terracciano, S.E. Harding, M.M. Stevens, Auxetic cardiac patches with tunable mechanical and conductive properties toward treating myocardial infarction, Adv. Funct. Mater. 28 (21) (2018) 1800618, https://doi.org/10.1002/adfm.201800618.

[54] X. Hu, P. Zhang, J. Liu, H. Guan, R. Xie, L. Cai, J. Guo, L. Wang, Y. Tian, X. Qiu, A Self-Association Cross-Linked conductive zwitterionic hydrogel as a myocardial patch for restoring cardiac function, Chem. Eng. J. 446 (2022) 136988, https://doi.org/10.1016/j.cej.2022.136988.

[55] A. Mihic, Z. Cui, J. Wu, G. Vlacic, Y. Miyagi, S.H. Li, S. Lu, H.W. Sung, R.D. Weisel, R.K. Li, A conductive polymer hydrogel supports cell electrical signaling and improves cardiac function after implantation into myocardial infarct, Circulation 132 (8) (2015) 772–784, https://doi.org/10.1161/circulationaha.114.014937.

[56] S. Zong, H. Lv, C. Liu, L. Zhu, J. Duan, J. Jiang, Mussel inspired Cu-tannic autocatalytic strategy for rapid self-polymerization of conductive and adhesive hydrogel sensors with extreme environmental tolerance, Chem. Eng. J. 465 (2023) 142831, https://doi.org/10.1016/j.cej.2023.142831.

[57] N.R. Alluri, N.P. Maria Joseph Raj, G. Khandelwal, V. Vivekananthan, S.-J. Kim, Aloe vera, A tropical desert plant to harness the mechanical energy by triboelectric and piezoelectric approaches, Nano Energy 73 (2020) 104767, https://doi.org/10.1016/j.nanoen.2020.104767.

[58] S.S. Dhadwar, T. Bemman, W.A. Anderson, P. Chen, Yeast cell adhesion on oligopeptide modified surfaces, Biotechnol. Adv. 21 (5) (2003) 395–406, https://doi.org/10.1016/s0734-9750(03)00056-9.

[59] H. He, H. Li, A. Pu, W. Li, K. Ban, L. Xu, Hybrid assembly of polymeric nanofiber network for robust and electronically conductive hydrogels, Nat. Commun. 14 (1) (2023) 759, https://doi.org/10.1038/s41467-023-36438-8.

[60] S.-M. Kim, N. Kim, Y. Kim, M.-S. Baik, M. Yoo, D. Kim, W.-J. Lee, D.-H. Kang, S. Kim, K. Lee, M.-H. Yoon, High-performance, polymer-based direct cellular interfaces for electrical stimulation and recording, NPG Asia Mater. 10 (4) (2018) 255–265, https://doi.org/10.1038/s41427-018-0014-9.

[61] J. Lee, V. Manoharan, L. Cheung, S. Lee, B.H. Cha, P. Newman, R. Farzad, S. Mehrotra, K. Zhang, F. Khan, M. Ghaderi, Y.D. Lin, S. Aftab, P. Mostafalu, M. Miscuglio, J. Li, B.B. Mandal, M.A. Hussain, K.T. Wan, X.S. Tang, A. Khademhosseini, S.R. Shin, Nanoparticle-based hybrid scaffolds for deciphering the role of multimodal cues in cardiac tissue engineering, ACS Nano 13 (11) (2019) 12525–12539, https://doi.org/10.1021/acsnano.9b03050.

[62] W. Xiong, X. Wang, H. Guan, F. Kong, Z. Xiao, Y. Jing, L. Cai, H. Hou, X. Qiu, L. Wang, A vascularized conductive elastic patch for the repair of infarcted myocardium through functional vascular anastomoses and electrical integration, Adv. Funct. Mater. 32 (19) (2022) 2111273.

[63] Y. He, H. Hou, S. Wang, R. Lin, L. Wang, L. Yu, X. Qiu, From waste of marine culture to natural patch in cardiac tissue engineering, Bioact. Mater. 6 (7) (2021) 2000–2010, https://doi.org/10.1016/j.bioactmat.2020.12.011.

[64] R. Bao, B. Tan, S. Liang, N. Zhang, W. Wang, W. Liu, A π-π conjugation-containing soft and conductive injectable polymer hydrogel highly efficiently rebuilds cardiac function after myocardial infarction, Biomaterials 122 (2017) 63–71, https://doi.org/10.1016/j.biomaterials.2017.01.012.

[65] D. Qu, J. Han, H. Ren, W. Yang, X. Zhang, Q. Zheng, D. Wang, Cardioprotective effects of Astragalin against myocardial ischemia/reperfusion injury in isolated rat heart, Oxid. Med. Cell. Longev. 2016 (2016) 8194690, https://doi.org/10.1155/2016/8194690.

[66] Q. Zhou, D. Meng, F. Li, X. Zhang, L. Liu, Y. Zhu, S. Liu, M. Xu, J. Deng, Z. Lei, J.P. G. Sluijter, J. Xiao, Inhibition of HIPK2 protects stress-induced pathological cardiac remodeling, EBioMedicine 85 (2022) 104274, https://doi.org/10.1016/j.ebiom.2022.104274.

[67] Z. Liao, Y. Chen, C. Duan, K. Zhu, R. Huang, H. Zhao, M. Hintze, Q. Pu, Z. Yuan, L. Lv, H. Chen, B. Lai, S. Feng, X. Qi, D. Cai, Cardiac telocytes inhibit cardiac microvascular endothelial cell apoptosis through exosomal miRNA-21-5p-targeted cdip1 silencing to improve angiogenesis following myocardial infarction, Theranostics 11 (1) (2021) 268–291, https://doi.org/10.7150/thno.47021.

[68] H. Shi, T. Xue, Y. Yang, C. Jiang, S. Huang, Q. Yang, D. Lei, Z. You, T. Jin, F. Wu, Q. Zhao, X. Ye, Microneedle-mediated gene delivery for the treatment of ischemic myocardial disease, Sci. Adv. 6 (25) (2020) eaaz3621, https://doi.org/10.1126/sciadv.aaz3621.

[69] P. Humbert, M. Brennan, N. Davison, P. Rosset, V. Trichet, F. Blanchard, P. Layrolle, Immune modulation by transplanted calcium phosphate biomaterials and human mesenchymal stromal cells in bone regeneration, Front. Immunol. 10 (2019) 663, https://doi.org/10.3389/fimmu.2019.00663.

[70] A.J. Mouton, X. Li, M.E. Hall, J.E. Hall, Obesity, hypertension, and cardiac dysfunction: novel roles of immunometabolism in macrophage activation and inflammation, Circ. Res. 126 (6) (2020) 789–806, https://doi.org/10.1161/circresaha.119.312321.

[71] J. Jang, H.J. Park, S.W. Kim, H. Kim, J.Y. Park, S.J. Na, H.J. Kim, M.N. Park, S. H. Choi, S.H. Park, S.W. Kim, S.M. Kwon, P.J. Kim, D.W. Cho, 3D printed complex tissue construct using stem cell-laden decellularized extracellular matrix bioinks for cardiac repair, Biomaterials 112 (2017) 264–274, https://doi.org/10.1016/j.biomaterials.2016.10.026.

[72] F. Pati, J. Jang, D.H. Ha, S. Won Kim, J.W. Rhie, J.H. Shim, D.H. Kim, D.W. Cho, Printing three-dimensional tissue analogues with decellularized extracellular matrix bioink, Nat. Commun. 5 (2014) 3935, https://doi.org/10.1038/ncomms4935.

[73] Y. Wu, L. Wang, B. Guo, P.X. Ma, Interwoven aligned conductive nanofiber yarn/hydrogel composite scaffolds for engineered 3D cardiac anisotropy, ACS Nano 11 (6) (2017) 5646–5659, https://doi.org/10.1021/acsnano.7b01062.